UNIVERSITÀ POLITECNICA DELLE MARCHE

DIPARTIMENTO DI SCIENZE DELLA VITA E

DELL'AMBIENTE

LAUREA MAGISTRALE – BIOLOGIA MARINA

"Ciclo Del Carbonato Di Calcio Nell'Oceano Indiano"

"Indian Ocean Calcium Carbonate Cycle"

Tesi di Laurea
di: Vanessa Cavucci

Vanessa Cavucci

Docente Referente
Chiar.mo Prof. Alessandra Negri

Chiar.mo Prof. Gianluca Marino

Contents

Abstract

Over the Late Pleistocene pCO_2 has varied in step with glacial/interglacial (G-IG). The causes behind these fluctuations are assessed but are hypothetically related to the calcium carbonate ($CaCO_3$) marine system, and the deep-water circulation changes. The $CaCO_3$ cycle is directly controlling the total alkalinity in the ocean, which is tightly related to the capacity of the ocean to act as a sink for pCO_2. To assess the causes behind the fluctuations of pCO_2, is important to investigate: the fluctuations in $CaCO_3$ contents of deep-sea sediments, and the response of dissolution proxies over G-IG periods in different ocean basins. Sediments from the Indian Ocean were poorly investigated and their results controversial. This work aimed at the reconstruction of the $CaCO_3$ weight percentage (wt.%) record from sediments of core U1443 in the equatorial Indian Ocean, that span the last 460,000 years, and to the comprehension of its fluctuation in the frame of G-IG cycles. Moreover, was verified the suitability of the revised size index as a dissolution proxy on sediments above lysocline. Measures of $CaCO_3$ contents in sediments were compared with proxies of paleo temperature ($\delta^{18}O$), relative terrigenous input and organic carbon export (log (Ba/Ti)), relative terrigenous input and $CaCO_3$ export, and with sedimentation rate. The revised size index results were compared

with values of a dissolution proxy applied on Site 758, of which core U1443 is a redrill. From the analysis conducted, it was found that the $CaCO_3$ wt.% record is not rank correlated with $\delta^{18}O$, thus indicating the absence of apparent in phase variations with G-IG cycles. Instead, the $CaCO_3$ wt.% has shown a strong positive rank correlation with log (Ba/Ti), and log (Ca/Terr) proxies ($p \leq 0.01$; $r_s = 0.44$, $r_s = 0.69$). Thus, suggesting that surface primary productivity by $CaCO_3$-secreting organisms, and terrigenous dilution mainly control the fluctuations of $CaCO_3$ wt.% in these sediments. Moreover, the strong positive linear correlation between log (Ba/Ti), and log (Ca/Terr) ($p \leq 0.01$; r^2=0.66), implies the 1:1 deposition ratio of Corg:Cinorg. Hence, it is dubious the effect of consistent pore water dissolution in these sediments. In the interval MIS 11 was observed the absence of a strong relationship between log (Ba/Ti) and $CaCO_3$ wt.%, which possibly means an increase effect of dissolution on the $CaCO_3$ wt.% record. Finally, results of the revised size index measured on sediments from above lysocline, compared with data of dissolution proxy from Site 758 shows disagreement. It is probably understandable as a lack of sensitivity of the revised size index on sediments above the lysocline depth.

Riassunto

Nel corso del Pleistocene superiore, il pCO_2 ha subito importanti fluttuazioni tra glaciale/interglaciale (G-IG). Le cause scatenanti queste fluttuazioni non sono del tutto chiare, ma si ritiene che siano correlate al ciclo del $CaCO_3$ ed a variazioni nella circolazione di masse d'acqua profonde. Il ciclo $CaCO_3$ ha un controllo diretto sull'alcalinità totale dell'oceano, la quale è relazionata con la capacità dell'oceano di assorbire il pCO_2. Per valutare le cause alla base delle fluttuazioni del pCO_2, è importante indagare le fluttuazioni del contenuto di $CaCO_3$ nei sedimenti di acque profonde, insieme con l'utilizzo di proxy di dissoluzione, in periodi G-IG nei diversi bacini oceanici. I sedimenti dell'Oceano Indiano non sono stati oggetto di numerosi studi e i risultati ottenuti da questi ultimi spesso controversi. In questo studio, i sedimenti provenienti da una carota dell'Oceano Indiano equatoriale (Site U1443), che copre gli ultimi 460,000 anni, verranno analizzati. Lo scopo è quello di ricostruire un record ad elevata risoluzione temporale della percentuale in peso di $CaCO_3$ (wt.%) e comprendere se le sue fluttuazioni sono fortemente relazionate con i cicli orbitali caratteristici del G-IG degli ultimi 460,000 anni. Inoltre, sono esaminate le relazioni tra le variazioni del $CaCO_3$(wt.%) e le condizioni di produttivita primaria, diluizione e dissoluzione del

Sito U1443. In questo studio viene inoltre verificata l'idoneità di un nuovo indice di dimensione come proxy di dissoluzione in sedimenti al di sopra del lisoclino. Per la verifica dei suddetti obiettivi, i risultati ottenuti delle misurazioni del contenuto di $CaCO_3$ sono stati confrontati con proxy di paleo temperatura ($\delta^{18}O$), di flusso relativo di materiale terrigeno e carbonio organico (log (Ba/Ti)), di flusso relativo di materiale terrigeno e $CaCO_3$ (log (Ca/Terr) e con i tassi di sedimentazione. Per quanto riguarda l'indice di dimensione, i risultati sono stati confrontati con quelli di un proxy di dissoluzione applicato nel sito 758, di cui il core U1443 è un redrill. Dall'analisi condotta è emerso che il $CaCO_3$ wt. % record non è correlato al $\delta^{18}O$, indicando così l'assenza di fluttuazioni di $CaCO_3$ wt. % in fase con cicli G-IG. Invece, il $CaCO_3$ wt. % ha mostrato una significativa correlazione di rank positiva con i proxy log (Ba/Ti) e log (Ca/Terr) ($p \leq 0.01$; $r_s = 0.44$, $r_s = 0.69$); suggerendo che la produttività primaria di superficie da parte degli organismi che secernono $CaCO_3$ e la diluizione terrigena sono i principali fattori che controllano le fluttuazioni del $CaCO_3$ wt. % in questi sedimenti. Inoltre, la significativa correlazione lineare positiva tra log (Ba/Ti) e log (Ca/Terr) ($p \leq 0.01$; $r^2 = 0.66$), implica un rapporto di deposizione 1:1 tra carbonio organico e carbonio inorganico. Quindi, è dubbio l'effetto consistente di una dissoluzione interstiziale in questi sedimenti. Nell'intervallo MIS 11 è stata osservata l'assenza

di una forte relazione tra log (Ba/Ti) e $CaCO_3$ wt. %, il che potrebbe essere dovuto ad un aumento dell'effetto di dissoluzione sul record di $CaCO_3$ wt. %. Infine, dal confronto tra i risultati dell'indice di dimensione con i risultati del proxy di dissoluzione misurato nel sito 758, è emerso un disaccordo. Questo è probabilmente dovuto ad una scarsa sensibilità dell'indice di dimensione nel fungere da proxy di dissoluzione in sedimenti al di sopra della profondità del lisoclino.

Chapter 1

INTRODUCTION

1.1 Overview on the role of $CaCO_3$ over the G-IG climate fluctuations in the-Late Pleistocene

During the last 1 million years of the Late Pleistocene, the climate suffered cyclical changes between periods of glacial (G) and interglacial (IG), expressed as an amplitude of ~100 ka (A. Berger, 1988; Colleoni et al., 2012). The so-called glacial-interglacial (G-IG) cycles – are characterized by larger volumes of continental ice and colder global and notably polar temperatures during G periods and warmer temperatures and lower ice volume during IG periods (A. Berger, 1988). Orbital changes related to incident solar radiation are the main factor triggering the shift between G-IG periods, but the only energy budget of changes in solar incidence is not enough. Indeed, another factor which might act as a coadjutant is the atmospheric CO_2 (pCO_2), enhancing the orbital effects through positive feedback. Records of air bubbles trapped in the Antarctic ice cores show that the concentrations of atmospheric CO_2 has varied in step with G-IG stages with, respectively, values of ~180-200 parts per million volumes (ppmv) and 280 ppmv (Brunelle et al., 2010; Petit et al., 1999). What could be the cause of the difference in 80 ppmv between G-IG cycles is still a matter of debate. Broecker, (1982) was the first to

assess that oceanic changes must underline the G-IG cycles in atmospheric CO_2. The reason lies on the role of the carbonate marine cycle in shaping the atmospheric and oceanic inventories of carbon over 1,000 to 100,000-year timescales, hence being potentially important in the G-IG climate changes during the Quaternary (Zeebe, 2012). It was established that carbonate burial during Quaternary shows cyclic variations over glacial/interglacial cycles, due to changes in biological production, deep-sea sequestration of respired CO_2, ocean circulation and sea level fluctuations (Arrhenius, 1952; Divakar Naidu et al., 1993; Peterson & Prell, 1985; Wood et al., 2023). Many of the nowadays considered theories which want to explain the pCO_2 fluctuations in the Quaternary need a better understanding of the $CaCO_3$ response during this period. The sediment content of $CaCO_3$ over different Ocean basins shows different responses over G-IG, with increased dissolution during interglacial and enhanced preservation during glacial in the Pacific ('Pacific pattern'), and opposite responses in the Atlantic ('Atlantic pattern') (Bassinot et al., 1994; Peterson & Prell, 1985). Instead, the Indian Ocean, in the middle way of the overturning thermohaline circulation, shows conflicting records, with some of them showing the 'Pacific Pattern', while others the 'Atlantic pattern' (Bassinot et al., 1994; Naik & Naidu, 2016; Peterson & Prell, 1985). The understanding of the dissolution and preservation pattern of the different Ocean

basins which would happened over G-IG cycles is of main concern to assess which of the principal hypotheses already presented could explain the pCO_2 fluctuations in the Quaternary (Archer et al., 2000; Brunelle et al., 2010; Sigman & Boyle, 2000).

1.2 Carbonate in the ocean sedimentation frame

$CaCO_3$ is an important component of marine sediments, of which deep-ocean pelagic sediments account for the most area and volume. Pelagic sediments are represented by deep-water pelagic clay and biogenic oozes. The latter is the result of settling material derived by productivity of pelagic organisms in the photic zone. While the pelagic clay is the result of local remobilization of sediments as turbidites (if adjacent to the continental slope), wind-blown materials originated from continental weathering or volcanic ash and cosmogenic dust depositions. The pelagic clay in the open ocean has usually a slow deposition rate (0.1 – 0.5 $cm\ kyr^{-1}$) but if the distance from the continental margin gets closer, the deposition rate can increase and become less stable in time (Rothwell, 2004). The biogenic oozes are classified considering the major percentage of the material composition: in siliceous (i.e., diatoms, etc.), or carbonate ooze (i.e., foraminifera, etc.). The deposition rate of calcareous sediments is usually bigger than the pelagic clay deposition ranging around (0.3 – 5 $cm\ kyr^{-1}$) and it is also less stable in time

because it also depends on primary productivity, so from the environmental features of the above photic layers (Rothwell, 2004). When nutrient availability in the photic zone is low, the production of $CaCO_3$ prevails over that of silica. This is the case of the oligotrophic tropical waters where coccolithophores production is high, and the food chain has a high number of trophic levels with small foraminifera feeding on nannoplankton coccolithophores. The calcareous detrital sinks into the ocean floor as fecal pellets or phytoplankton aggregates. Those particles are the main drivers of organic matter to the sea floor, so that the precipitation ratio between $CaCO_3$ and organic matter is usually 1:1 in an open ocean environment (Rothwell, 2004; Sarmiento & Gruber, 2006). Most of the organic matter gets utilized by bacterial metabolization and dissolves, increasing the concentration of dissolved organic matter and DIC due to the metabolic waste (CO_2). The carbonate particles can get dissolved if the surrounding waters are undersaturated in $CaCO_3$ while going through diagenesis process (into pelagic chalks, or limestone) if the surrounding environment is saturated in $CaCO_3$. The main factor controlling the saturation (undersaturation) of the surrounding waters is a thermodynamic factor, which mainly depends on pressure, triggering the dissolution with increasing depth. $CaCO_3$ in the marine environment exists in two main different mineral forms: aragonite and calcite. The carbonate saturation for these two mineral forms

is different and is due to their mineral structure. Aragonite is thermodynamically less stable than calcite, so it dissolves first in the water column (Broecker, 2003; Sarmiento & Gruber, 2006). The pelagic $CaCO_3$ production concerns both mineral forms, which production is by different marine organisms (Reijmer, 2021). Calcite production in the pelagic realm is the dominant one and has mayor relevance on large temporal and spatial scales than the aragonite one. In this work, whenever referring to $CaCO_3$ without specifying which form, it is understood that is the calcite mineral form.

1.3 Marine carbonate chemistry

The carbon dioxide (CO_2) that dissolves in seawater exists in four inorganic forms:

(1) Free aqueous carbon dioxide ($CO_2(aq)$);

(2) Bicarbonate ion (HCO_3^-);

(3) Carbonate ion (CO_3^{2-});

(4) True carbonic acid (H_2CO_3).

The sum of $CO_2(aq)$ and H_2CO_3 is denoted as $[CO_2]$, while the sum of the dissolved carbonate species reported above is de-noted as total dissolved inorganic carbon (DIC):

$$DIC = [HCO_3^-] + [CO_3^{2-}] + [CO_2] \quad (1.1)$$

Brackets in equation 1.1 (and throughout the remainder of this thesis) indicate total stochiometric concentrations of the relevant chemical species. In the modern ocean: (*i*) HCO_3^- and CO_3^{2-} are the most (~89%) and the least abundant (~0.5%), of these chemical species, respectively; and (*ii*) the average concentration of DIC is ~2.3 mmol kg^{-1} (Zeebe & Wolf-Gladrow, 2001). Changes in the concentrations of CO_2, HCO_3^-, and CO_3^{2-} in seawater are generally represented as a function of its pH in the so-called Bjerrum plot (Figure 1.1). Seawater pH is defined as the negative logarithm of hydrogen ion (H^+) concentration:

$$pH = -\log[H^+] \tag{1.2}$$

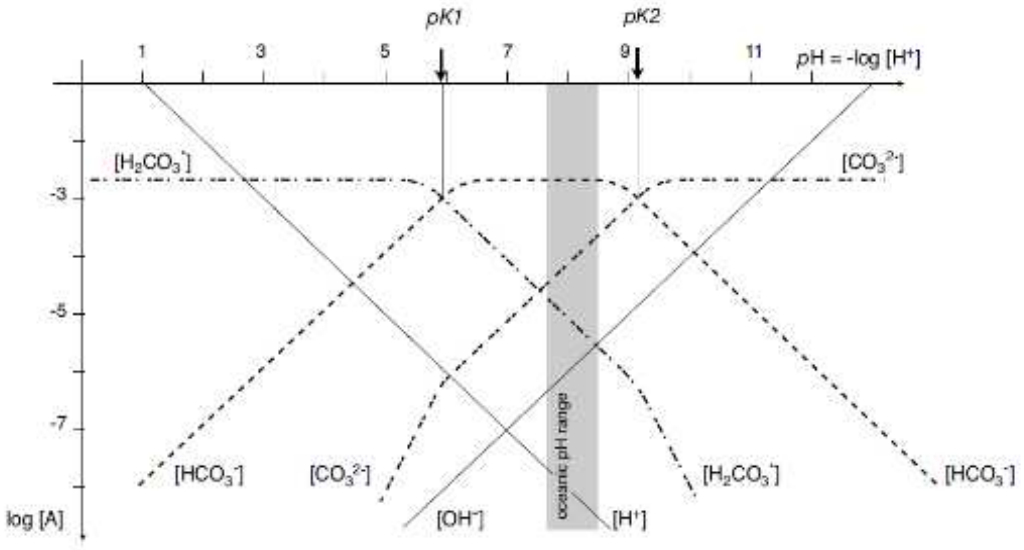

Figure 1.1 | Bjerrum plot. It represents changes in concentrations of the dissolved carbonate species in seawater as a function of pH, both expressed in logarithmic scale. The grey band indicates the oceanic pH range, modified from (Sarmiento & Gruber, 2006).

At typical surface ocean pH conditions (~8.1), the speciation between $[CO_2]$, $[HCO_3^-]$, and $[CO_3^{2-}]$ is 0.5%, 89%, and 10.5%, respectively. Accordingly, most of the DIC in the ocean is accounted for by HCO_3^- (Zeebe, 2012; Zeebe & Wolf-Gladrow, 2001). The addition of a strong acid to seawater would convert CO_3^{2-} to HCO_3^- and the latter in CO_2. This would confine pH changes between 8 and 6, making the carbonate system a buffer for seawater pH.

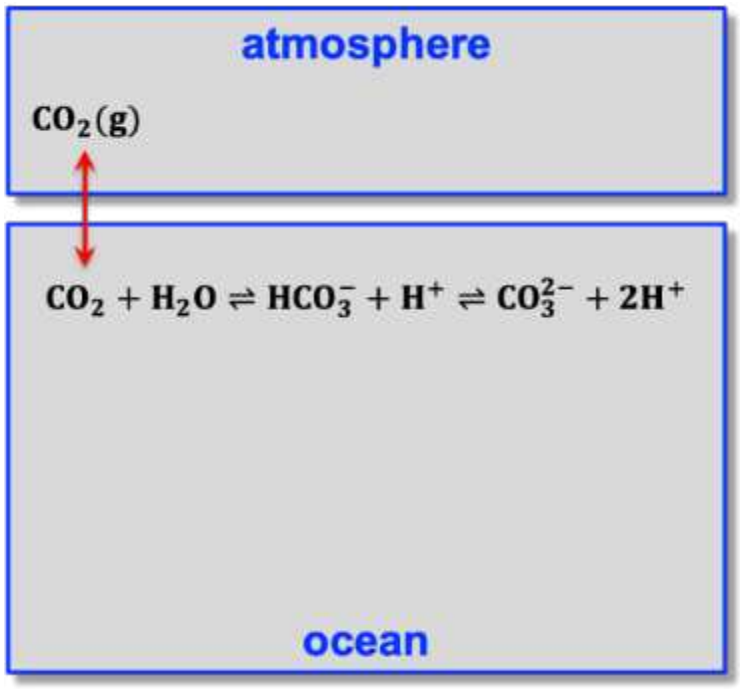

Figure 1.2 | Sketch of the oceanic carbonate system, whereby the exchange of CO_2 between the atmosphere and the ocean triggers a series of reactions that lead to the production of bicarbonate (HCO_3^-), carbonate (CO_3^{2-}), and hydrogen (H^+) ions (modified after Zeebe & Wolf-Gladrow, 2001).

Under conditions of thermodynamic equilibrium, the gaseous carbon dioxide ($CO_2(g)$) and $[CO_2]$ dissolved in seawater are related to one another by the Henry's law:

$$[CO_2(g)] \overset{K_0}{=} [CO_2] \tag{1.3}$$

where K_0 is the solubility coefficient of CO_2 in seawater (Weiss, 1974), which depends on both, ambient temperature and salinity. Specifically, solubility is higher (lower) in colder (warmer) and less (more) saline water. When gaseous $CO_2(g)$ dissolves in seawater, it first gets hydrated to form $CO_2(aq)$, which reacts with water to form H_2CO_3. H_2CO_3 then rapidly dissociates into HCO_3^-, which in turn dissociates into CO_3^{2-} (Figure 1.2). Both reactions re-lease protons into sea-water (hydrogen ions, H^+), thereby lowering seawater pH. Three equations de-scribe the (equilibrium) reaction of the dissolved carbonate species with water (H_2O), H^+, and hydroxyl ions (OH^-):

$$CO_2(g) + H_2O \hat{U} H_2CO_3 \tag{1.4}$$

$$H_2CO_3 \overset{K_1^*}{\Leftrightarrow} HCO_3^- + H^+ \tag{1.5}$$

$$HCO_3^- \overset{K_2^*}{\Leftrightarrow} CO_3^{2-} + H^+ \tag{1.6}$$

K_1^* and K_2^* are the first and second (equilibrium) dissociation constants of H_2CO_3 in seawater. The equilibrium relationships between these species are given by:

$$K_0 = \frac{[CO_2]}{pCO_2} \tag{1.7}$$

$$K_1^* = \frac{[HCO_3^-][H^+]}{[CO_2]} \tag{1.8}$$

$$K_2^* = \frac{[CO_3^{2-}][H^+]}{[HCO_3^-]} \tag{1.9}$$

The dissociation constants for acid-base reactions, as the ones above, are a quantitative measure of the acidic strength in a solution. They are calculated considering the concentrations of the acid and base species when they are at equilibrium. Higher is the value of K_1^*, and K_2^* and higher is the propensity of the reagent (acid species) to dissociate in the products (conjugate base and hydrogen ion, H^+). The dissociation constants are affected by changes in temperature, salinity, and strength of the ionic species. For practical purpose, the constants values are usually expressed in logarithmic scale:

$$pK_* = -\log K_* \tag{1.10}$$

For a salinity of 35 and a temperature between 0˚C and 30˚C, we have values ~6 for pK_1, and ~9 for pK_2. In the Bjerrum plot (Figure 1.1), they are represented as the same value of pH when the concentration of reagents and products are equal, considering the formulas (1.2), (1.8), (1.9), and (1.10). Which means that when

the pH value changes from the values correspondent to the values of pK_1, and pK_2 we would have an increase or decrease in the concentrations of reagents and products. More specifically, when there is an increase in the pH value we have an increase in the concentration of the reaction products while when pH decreases, we have an increase in the concentration of reagents (Sarmiento & Gruber, 2006). Another important parameter of the carbonate system is the total alkalinity (TA) a measure of the charge balance, defined as the excess of bases (proton acceptors) over acids (proton donors) (Dickson, 1981). Alkalinity is practically representing the buffer capacity of seawater. Since there are minor bases like phosphate, silicate, and sulphate which contribution to variation in alkalinity is less than one percent, we can neglect them and consider TA as:

$$\mathrm{TA} = [\mathrm{HCO_3^-}] + 2[\mathrm{CO_3^{2-}}] + [\mathrm{B(OH)_4^-}] + [\mathrm{OH^-}] - [\mathrm{H^+}] \qquad (1.11)$$

$$+ \text{ minor compounds}$$

The sum of the already introduced parameters (pH, DIC, TA, $p\mathrm{CO_2}$, $\mathrm{HCO_3^-}$, $\mathrm{CO_3^{2-}}$) are part of the carbonate system in marine seawater (Sarmiento & Gruber, 2006).

Two of these parameters must be known to determine the carbonate system. TA and DIC, differently from the other carbonate parameters are conservative quantities, which means that their concentrations are unaffected by changes in

pressure and temperature and obey the linear mixing law. Therefore, they are easier to utilize in numerical models of the ocean's carbon cycle to characterize the processes that impact the ocean carbonate system (Zeebe, 2012). Hence, DIC and TA are used for the determination of the other components of carbonate system (Sarmiento & Gruber, 2006). The [TA] and [DIC] are not homogenized in the water column, having both lower values at the surface water than the deep ocean water, with a greater difference in DIC concentrations between the two realms (Sarmiento & Gruber, 2006). These gradients are maintained by key components of the marine carbon cycle that are dubbed 'pumps' because they work against the chemical gradients in the ocean. In Figure 1.3, we can see the effects of these 'pumps' on TA and DIC concentrations, at constant temperature, pressure, and salinity. The 'physical pump' is a physical-chemical process which drives CO_2 exchange between the atmosphere, surface ocean, through the ocean interior and is driven by the global ocean. The invasion (release) of CO_2 in (out) the seawater determines an increase (decrease) in DIC but has no effect on alkalinity. The CO_2(g) is more soluble in cold waters, thus determining an invasion of this gas into the water, while at low latitudes whereas seawater temperature is higher the CO_2 gets mostly released from the ocean surface to the atmosphere.

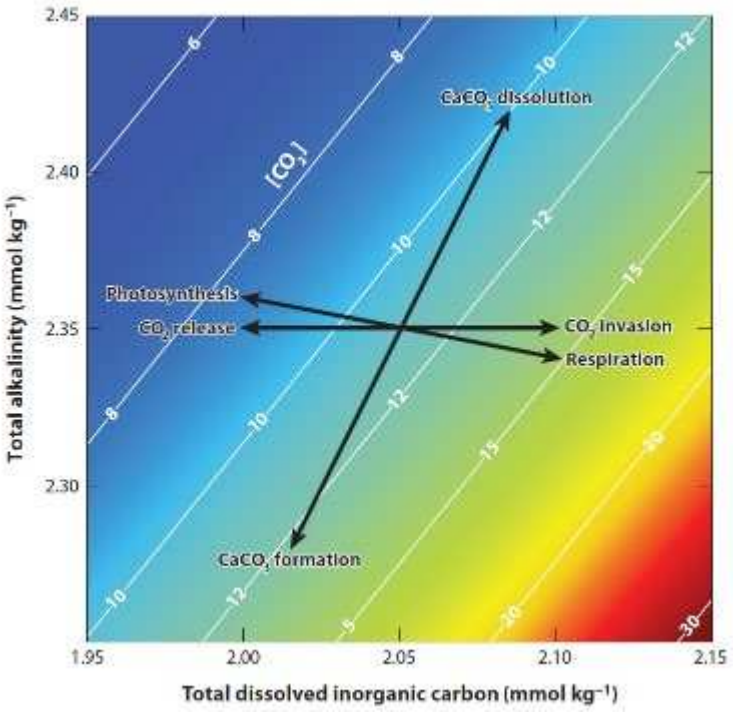

Figure 1.3| Effects of different processes of carbon cycle on [TA] and [DIC] expressed as mmol kg^{-1}. Parameters of temperature T= 15˚C, salinity S= 35, and pressure P= 1 atm . The constant concentrations of CO_2, expressed in µmol kg^{-1} are indicated with the diagonal lines. More details in the text. Picture modified by (Zeebe, 2012).

Moreover, another physical process is involved in transporting CO_2 throughout the ocean. The formation of dense water at high latitudes by downwelling transports CO_2 to the deep ocean compartments. By the action of thermohaline circulation these water masses transport the CO_2 through different ocean basins and again back to the surface ocean in the upwelling zones (Sarmiento & Gruber, 2006; Yu et al., 2014; Zeebe, 2012).

The 'biological pump' is linked to the respiration and photosynthesis by marine organisms, which lead to modification of [TA], and [DIC]. The CO_2 and nutrients upwell in the photic zone get utilized by autotrophic organisms to produce biomass and O_2 through photosynthesis. The production of organic matter by algae consumes CO_2 which makes the [DIC] decrease, while the up-take of nitrate (NO_3^-) by algae makes the [TA] increase (Yu et al., 2014; Zeebe, 2012). The 'carbonate counter-pump' involves the action of calcifying organisms on the precipitation of $CaCO_3$, and its dissolution reaction. The precipitation and dissolution reactions of $CaCO_3$ are as follows:

$$2HCO_3^- + Ca^{+2} \rightleftharpoons CO_2 + CaCO_3 + H_2O \qquad (1.12)$$

The name 'counter-pump' is because of the counterintuitive increase of $[CO_2]$ by the $CaCO_3$ precipitation reaction. The reason for the $[CO_2]$ increase is that the production of $CaCO_3$ decreases [DIC] and [TA] in a 1:2 ratio (Figure 1.3). Hence, a reduction in [TA] means a reduction in the total buffering capacity of the ocean, which makes the medium more acidic and the concentration of dissolved CO_2 to increase (Figure 1.1) (Sarmiento & Gruber, 2006; Zeebe, 2012).

1.4 Production of $CaCO_3$ in the ocean

The total production of the mineral $CaCO_3$ in the marine environment and its

sedimentation leads to the formation of two main types of carbonate sediments. Those precipitated by the production of carbonate by benthic organisms which are found on the continental shelf and reefs, and those precipitated by planktonic organisms that post-mortem settle through the water column and form the deep ocean carbonate oozes. The production rate of $CaCO_3$ is way faster for benthic organisms than planktonic organisms, but the contribution to the total amount of $CaCO_3$ production is bigger for the latter, with values of $42 \cdot 10^{12} \text{mol yr}^{-1}$ and $133 \cdot 10^{12} \text{mol yr}^{-1}$, respectively (Smith & Mackenzie, 2016).

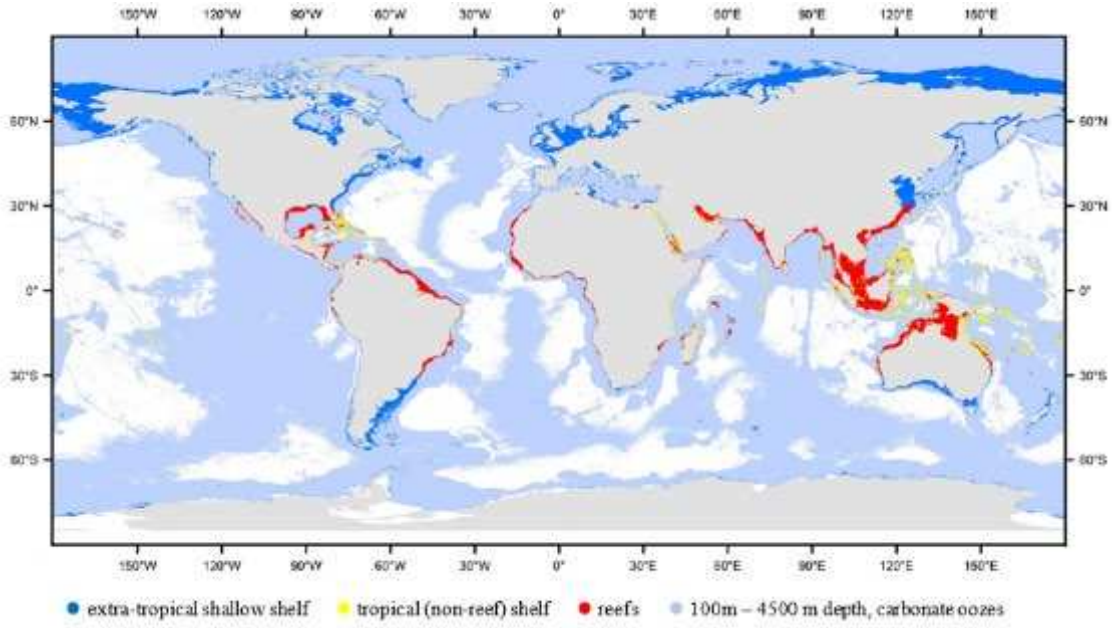

Figure 1.4| Global distributions of marine carbonate sediments. In the text, extra-tropical shallow shelf, tropical (non-reef) shelf, and reefs are referred to as shelf carbonate sediments. Picture modified from (Smith & Mackenzie, 2016).

The reason for the greater contribution by the planktonic production to the total budget of $CaCO_3$ is the larger area occupied by the deep carbonate oozes than by the shelf carbonate deposits (Figure 1.4) (Smith & Mackenzie, 2016). In the open ocean, the $CaCO_3$ production is almost exclusively due to biological processes which take place in the photic zone of the ocean, by three main groups of organisms. These groups are coccolithophores, foraminifera, and pteropods. Pteropods are part of a group of pelagic gastropods which secretes aragonite shells. The pteropod shells in the Atlantic Ocean dissolve before reaching the 2500 m depth while in the Indian/Pacific Ocean above 1500 m depth (Rothwell, 2004). Differently, coccolithophores and foraminifera possess structures made of calcite. Coccolithophores are unicellular protist members of the group Haptophyceae that belong to the class Prymnesiophyceae (Tyrrell & Young, 2009).

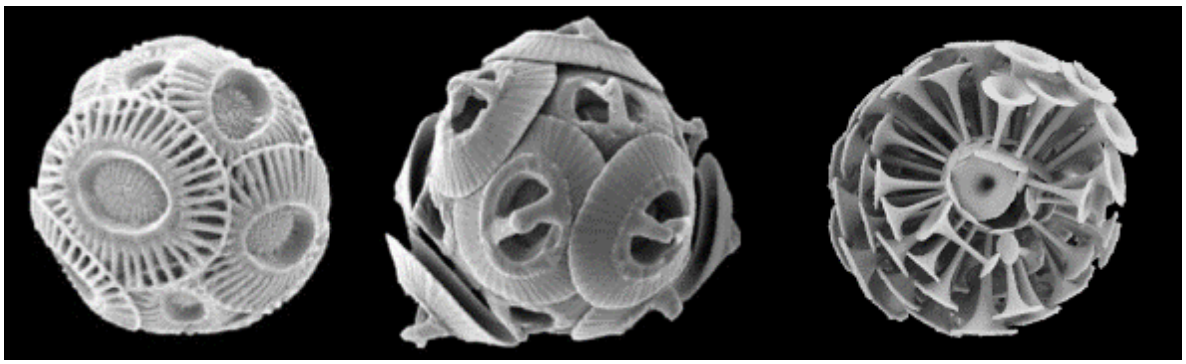

Figure 1.5| Scanning electronic microscope picture of different coccolithophore species. From the left to the right: *Emiliana huxleyi, Gephyrocapsa oceanica,* and *Discosphaera tubifera*, re-adapted from (Sarmiento & Gruber, 2006).

They are covered by an exoskeleton of calcite around the cell, the coccosphere which diameter varies between 5 to 100 μm (Arundhathy et al., 2021). The coccosphere is the union of many different $CaCO_3$ plates named coccoliths, which get produced within the cell and then expelled outside it. The coccolith typical size is around 2 to 25 μm (Arundhathy et al., 2021; Tyrrell & Young, 2009). These unicellular organisms are ubiquitous in the ocean, but they seem to prefer low-nutrient, low-latitude, optimum-temperature ecosystems which match with the environmental features of the Indian Ocean (Armstrong & Brasier, 2013; Arundhathy et al., 2021). Some of the most important species at low latitudes are *Emiliana huxleyi*, *Gephyrocapsa oceanica*, *Calcidiscus leptoporus*, *Helicosphaera carterae*, and *Discosphaera tubifera* (Figure 1.5). Coccoliths are the first constituents of deep carbonate oozes. Seconds in this ranking are foraminifera, which nowadays contributes together with coccoliths to the 80 % of carbonate depositions in the entire ocean (Armstrong & Brasier, 2013). Foraminifera is a group of unicellular protozoans included in the phylum of Rhizopoda. They can live either in the planktonic or benthonic environment. The soft tissue of their cells is mostly enclosed in a shell or test, which in a wide number of species is composed of the mineral calcite. These tests consist of several hollow chambers mostly interconnected with each other, which are produced sequentially as the organism grows.

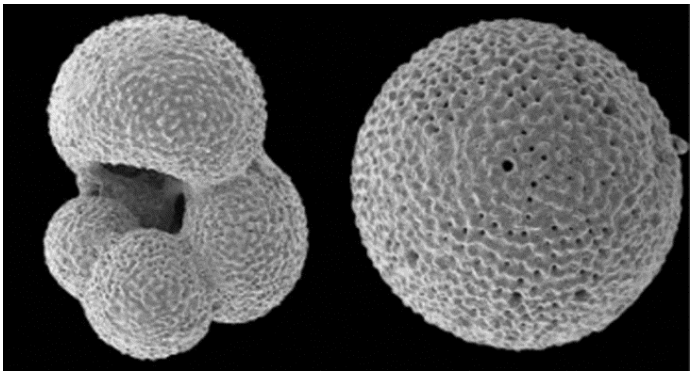

Figure 1.6| Scanning electron microscope picture of *Globigerinella calida* on the left and *Orbulina universa* to the right, modified from (Öğretmen et al., 2018).

There are around 100 species of living planktonic foraminifera, which size tend to be <100 μm (Armstrong & Brasier, 2013). The diversity and number of endemic species increase towards tropical latitudes. Some of the most characteristic species of these latitudes are *Globigerinoides ruber*, *Neogloboquadrina dutertrei*, *Trilobatus trilobus*, *Globorotalia* spp., and *Orbulina universa* (Figure 1.6).

1.5 Dissolution of $CaCO_3$ in the ocean

At the end of their life cycle, the $CaCO_3$ hard parts of foraminifera and coccolithophores, sink in the water column to reach the deep ocean compartment and finally the ocean floor where they could get buried. The particles that leave the ocean surface can either be dissolved in the water column or at the ocean floor, while about the 13 % of them get finally buried (Sarmiento & Gruber, 2006). The

dissolution of $CaCO_3$ is dependent on the saturation state of the surrounding seawaters (Sarmiento & Gruber, 2006). Saturation state for $CaCO_3$, here in after indicated as Ω, is measured considering the observed $[CO_3^{2-}]$, $[Ca^{+2}]$, and the in-situ solubility product of $CaCO_3$ (Ksp^{CaCO_3}):

$$Ksp^{CaCO_3} = [CO_3^{2-}]_{sat}\left[Ca^{2+}\right]_{sat} \quad (1.13)$$

$$\Omega = \frac{[CO_3^{-2}][Ca^{+2}]}{Ksp^{CaCO_3}} \quad (1.14)$$

The $[Ca^{+2}]$ is usually considered constant because its concentration in the ocean is three orders of magnitude higher than $[CO_3^{-2}]$, and so variation in its concentration is very small related to those of $[CO_3^{-2}]$, hence the Ω can be revised in:

$$\Omega \approx \frac{[CO_3^{-2}]}{Ksp^{CaCO_3}} \quad (1.15)$$

The solubility product is mostly pressure dependent, increasing with water depth, while temperature and salinity have a smaller effect. The dissolution of $CaCO_3$ takes place where the seawater is undersaturated (Ω<1), while precipitation happens where seawater is saturated in $CaCO_3$ (Ω>1). Hence, any processes which makes change either the Ksp^{CaCO_3} or the $[CO_3^{-2}]$, because of the formula (1.15) would determine a change in the saturation state of seawater and possible

dissolution (precipitation) of $CaCO_3$. The water depth at which the Ω=1 is termed the calcite saturation horizon or calcite saturation depth (CSD) and is a water column property (Figure 1.7) (Sarmiento & Gruber, 2006; Zeebe, 2012). As already said, the solubility product increases with water depth. Indeed, $CaCO_3$ sediment plots against water depth, of all the ocean basins, show the same pattern. The mid-depth sediments rich in $CaCO_3$ and abyssal sediments avoid in $CaCO_3$ (Broecker, 2003; Sarmiento & Gruber, 2006).

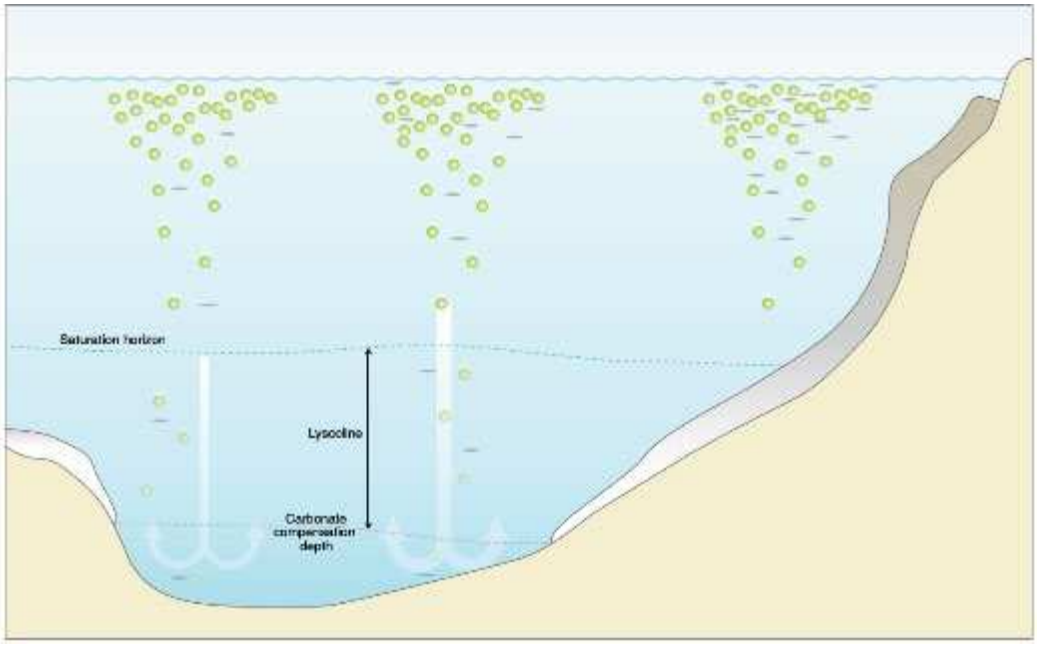

Figure 1.7| Schematic representation of the precipitation of $CaCO_3$ produced in the photic zone (green circles), and lithogenic material (grey plates). The calcite saturation horizon, and the calcite compensation horizon are highlighted by dot lines. The lysocline here identified as transition zone is highlighted. Picture modified from (Boudreau et al., 2018).

Between these two realms is the ‘transition zone’, which the upper limit is the ‘lysocline’ and the lower limit is the ‘calcite compensation depth’ (CCD) (Broecker, 2003; Sarmiento & Gruber, 2006). The lysocline is the depth at which the dissolution impact becomes evident (as a decrease of carbonate percentages), while the CCD is operationally defined as the depth where the weight percent of $CaCO_3$ in sediments is around 2 or 10% (Zeebe, 2012). At the CCD depth the rain rate of $CaCO_3$ equals the dissolution rate. The previous definitions of CSD, CCD, and lysocline are vastly used in past works on the Indian Ocean and due to a practical purpose, I will use the same definition in the present work. But it should be noted, that the most recent definition of the term lysocline identifies it as a transition zone between the CSD and the CCD (Boudreau et al., 2018) (Figure 1.7). However, waters exceeding the CSD are not the only ones exposed to changes in the saturation state of calcite. Indeed, metabolic remineralization of organic matter, which has as a waste product $[CO_2]$ would decrease the $[CO_3^{-2}]$ of the surrounding seawater, possibly triggering the $CaCO_3$ dissolution in the interstitial waters above and below the CSD.

1.5.1 Water column dissolution

The dissolution of $CaCO_3$ in the water column accounts for the 50 % of the initial export of $CaCO_3$ from the surface ocean (Sarmiento & Gruber, 2006). Several

studies conducted to assess the degree of dissolution on settling $CaCO_3$ particles (Martin et al., 1993; Milliman et al., 1999), reveals that the majority of water column dissolution happens before the 1000 m depth, which corresponds to the realm of saturated waters respect to the high Mg calcite. Hence, being the mineral aragonite only the 10 % of the total initial export, the 50 % dissolution of total $CaCO_3$ export above the calcite saturation horizon should be triggered by other processes than the only aragonite dissolution (Sarmiento & Gruber, 2006). Mechanisms which involve biological transformations by acidic guts of grazers and remineralization of organic matter on settling $CaCO_3$ particles seem to be relevant in the water column dissolution processes (Fiadeiro, 1980). The dissolution in the water column due to the passage of $CaCO_3$ particles below the calcite saturation horizon is actually small (Broecker, 2003; Sarmiento & Gruber, 2006). This depends on the high settling velocity of $CaCO_3$ particles, which reduces the time they spend in the undersaturated waters, and on its slow dissolution kinetics (Sarmiento & Gruber, 2006).

1.5.2 Sediment dissolution

The particles which over-pass the dissolution in the water column can either get buried (~13 % of the initial $CaCO_3$ export) or dissolved. The deep undersaturated waters expose the interface sediment to dissolution. Sediment dissolution

processes are mostly driven by thermodynamic. Indeed, over the different ocean basins the calcite saturation horizon is consistent with the lysocline depth (Sarmiento & Gruber, 2006). The calcite saturation horizon is 1 km deeper in the Atlantic Ocean than Pacific/Indian Ocean and so is the average lysocline. It is interesting to notice that the transition zone is not the same amplitude over oceans (Figure 1.8), and that the average $CaCO_3$ content for a given value of Ω is not the same between the Atlantic and Pacific/Indian (with 10 % lower values of $CaCO_3$ content in the Atlantic at the same values of Ω with the Pacific/Indian Ocean) (Sarmiento & Gruber, 2006). The last preservation features are not directly related to the calcite saturation horizon itself but are dependent on the rain rate of inorganic non carbonate material, carbonate rain itself, and rain ratio of organic-to-inorganic fraction (Sarmiento & Gruber, 2006). The organic matter sinks onto the sediment floor mostly transported by $CaCO_3$ particles and gets quickly remineralized. It changes the carbonate saturation state of pore waters, decreasing the concentration of $[CO_3^{-2}]$ independently of the overlying waters saturation state. Since the dissolution and remineralization have almost opposite effect on $[CO_3^{-2}]$, a rain ratio of organic-to-inorganic matter in the order of 1:1 or higher is necessary to bring the $CaCO_3$ to complete dissolution. Although the organic matter deposition in shallower waters is usually bigger, there is not any substantial dissolution. The

reason for this none dissolution is that at shallower depths, the protons produced by remineralization processes get buffered by the overlying supersaturated waters before they can cause any $CaCO_3$ dissolution, which reaction is quite slow. Archer, (1991), using a computational model, assessed the effects of the rain ratio of different origin materials on the transition zone and lysocline depth with respect to the calcite saturation horizon. It seems that the organic-to-inorganic rain ratio could regulate the distance between the lysocline and the calcite saturation horizon depth. With values of rain ratio equal 1:1 the lysocline is almost perfectly overlapping the calcite saturation horizon.

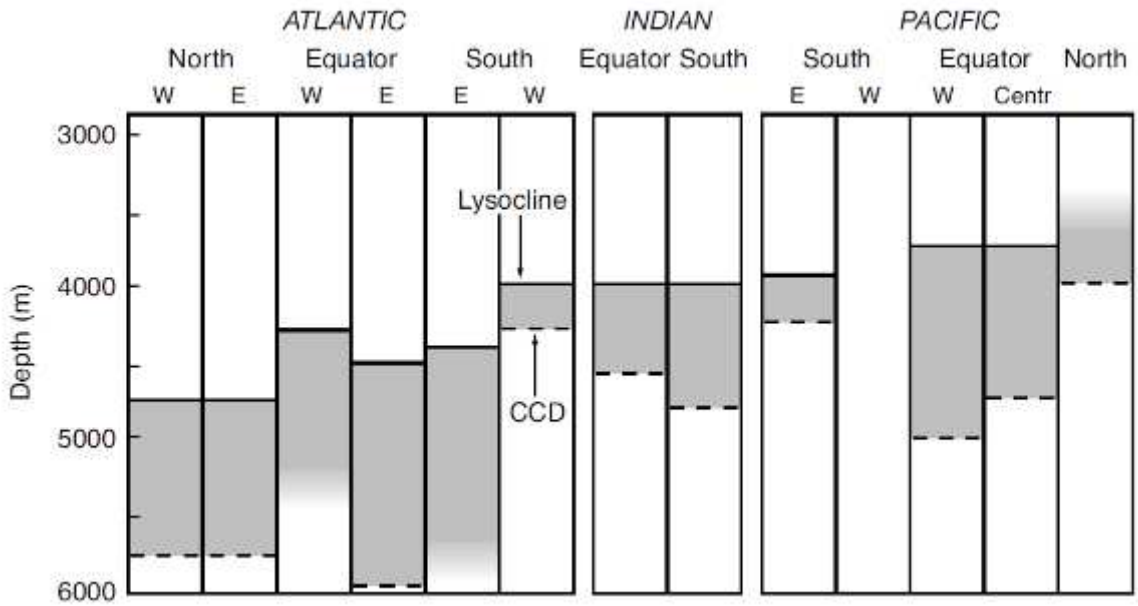

Figure 1.8| Atlantic, Indian, and Pacific representation of the different transition zone and related lysocline and CCD depths (Sarmiento & Gruber, 2006).

For values above 1:1, there is the possibility for the regional lysocline to exceed the calcite saturation horizon. The $CaCO_3$ rain rate, and the deposition of other detrital sediments, are responsible for the thickness of the transition zone. Indeed, new deposited material contributes to the downward advection of the sediments, which drives $CaCO_3$ more rapidly away from the undersaturated overlying waters (Sarmiento & Gruber, 2006). This is in line with what observed between the bigger Atlantic transition zone thickness in respect to the Pacific/Indian oceans. Indeed, the rain rate of non-$CaCO_3$ material is smaller in the Pacific and Indian Ocean (Figure 1.8)(Sarmiento & Gruber, 2006).

1.6 Carbonate ion distribution

The difference in the Ω between the Atlantic and Indo-Pacific oceans is caused by the differential distribution of the $[CO_3^{-2}]$ ion. Changes in the $[CO_3^{-2}]$ are related to the release (invasion) of CO_2, precipitation (dissolution) of $CaCO_3$, and photo-synthesis (respiration). The surface ocean is generally characterized by higher amounts of $[CO_3^{-2}]$ than the deep ocean. The concentration of carbonate ion can be approximated to be:

$$[CO_3^{-2}] \approx TA - DIC \tag{1.16}$$

Photosynthesis and remineralization have opposite effects on carbonate ion concentrations. The first increases TA by taking up nitrate while decreasing the DIC through consume of $[CO_2]$, hence determining an overall increase in $[CO_3^{-2}]$ (Yu et al., 2014). The remineralization process increases DIC by releasing $[CO_2]$, and decreases TA by transforming the organic nitrogen into nitrate, hence resulting in a decrease of $[CO_3^{-2}]$ (Sarmiento & Gruber, 2006). The general decrease in $[CO_3^{-2}]$ through the water column is due to the maximum photosynthesis extent in the photic zone and the remineralization processes happening inversely to the photosynthesis with maximum extent in the bottom ocean (Broecker, 2003; Sarmiento & Gruber, 2006). Although this is the general rule, over all oceans below the 1500 m depth, water masses' diffusion imposes secondary features to the general distribution (Broecker, 2003; Yu et al., 2014). The deep ocean waters are a mixture of two end members, the North Atlantic Deep Waters (NADW), and the Antarctic Bottom Waters (AABW). The NADW has the highest values of $[CO_3^{-2}]$ which is ~120 μmol kg^{-1} (Broecker, 2003; Yu et al., 2014). While the AABW have smaller values of carbonate ion which concentration is ~80 μmol kg^{-1} (Broecker, 2003; Yu et al., 2014) (Figure 1.9). This difference is due to the high primary productivity in the North Atlantic Ocean, against the incomplete nutrient utilization in the

Southern Ocean. Moreover, the latter is exposed to intensive upwelling that, together with the AABW formation, homogenize properties across the water column, allowing the remineralization products to reach the surface and further contributing to the lower concentration of carbonate ions in the water column. The release of $[CO_2]$ in the Southern Ocean and the uptake of $[CO_2]$ in the North Atlantic Ocean contribute to slightly decrease the difference in the carbonate ion concentration between the two water masses, which otherwise would be even larger (Broecker, 2003).

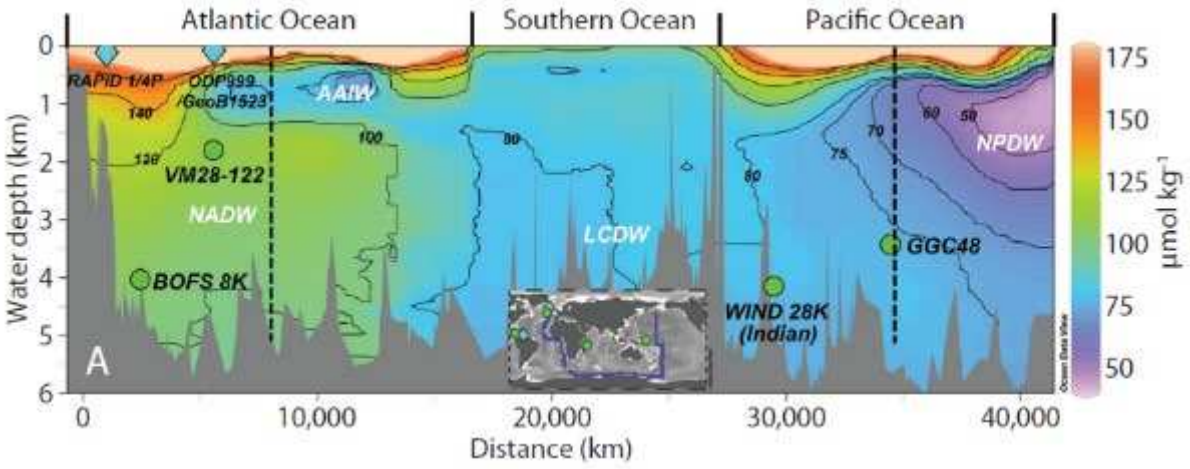

Figure 1.9 | Distribution of seawater $[CO_3^{-2}]$ in the modern ocean. The water masses initials are written in white in the image. (AAIW) Antarctic Intermediate Water, (NADW) North Atlantic Deep Water, (LCDW) Lower Circumpolar Deep Water and (NPDW) North Pacific Deep Water. Diamonds and circles indicate respectively the core site for surface and deep water $[CO_3^{-2}]$ reconstructions. Readapted from (Yu et al., 2014).

In the Southern Ocean, NADW mixes with the waters of the Southern Ocean and flows back northward to the Pacific, Indian and Atlantic Ocean as AABW, and Antarctic Intermediate Waters (AIW). The lowest value of $[CO_3^{-2}]$ ~50 μmol kg^{-1} is found in the deep North Pacific Ocean. This characteristic reflects the aging of the deep waters which from the North Atlantic Ocean to the North Pacific Ocean had accumulated the products of organic matter remineralization from the bottom ocean (Broecker, 2003; Yu et al., 2014). In the South Indian Ocean, and South Pacific Ocean the concentration of $[CO_3^{-2}]$ remained mostly unchanged with respect to those of the Southern Ocean. The reason is that the decrease in the $[CO_3^{-2}]$ due to water masses aging is almost perfectly balanced by its increase due to the dissolution of $CaCO_3$ (Broecker, 2003; Yu et al., 2014). This chemical titration is possible due to the vast depth of the Pacific, and Indian Ocean, which expose a major percentage of their sediments below the calcite saturation horizon and so to dissolution.

1.7 Long-term $CaCO_3$ *adjustment in the carbon cycle frame*

The main natural reservoirs of carbon (C) on Earth are characterized by different amounts of carbon and different exchange timescales (Figure 1.10). The atmosphere, the biosphere, the soils, and the surface ocean inventories account for ~3,600 [pentagrams of carbon (Pg C); 1 Pg= 10^{15} g], which represent only 10% of

the deep ocean reservoir ~38000 Pg C. The biggest reservoir is represented by the sediments and crust, with ~48,000,000 Pg C (Sigman & Boyle, 2000; Zeebe, 2012). Any of these inventories is related to the others by processes happening on different timescales. On decadal to centennial timescales, the atmosphere, the biosphere, and the surface ocean interchange carbon through different forms: $CO_{2(g)}$ in the atmosphere, organic carbon in the biosphere and DIC in the surface ocean.

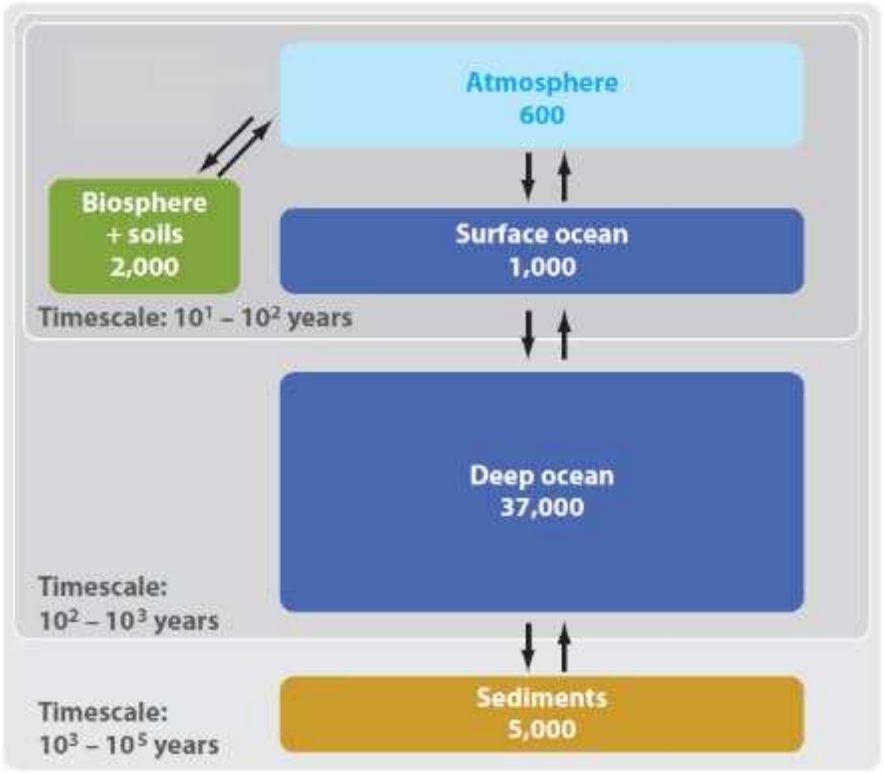

Figure 1.10| Schematic representation of the carbon cycle reservoirs, the amount of carbon is in pentagrams of carbon. The grey boxes enclose reservoirs involved in the carbon exchange and the respective timescales. Imagen modified from (Zeebe, 2012).

The DIC from the surface ocean gets exchanged with the deep ocean reservoirs of carbon over ~1000 years timescales, due to the transport by the great conveyor belt. On these timescales, both DIC and TA are mobilized between the different compartments of the ocean, but the total inventory does not change. On millennial to 100,000 timescales, the exchange of carbon happens between the reactive carbonate sediments and the DIC, and TA ocean inventories, by a process called 'calcite homeostat' (Broecker, 2003; Sarmiento & Gruber, 2006; Zeebe, 2012).

1.8 $CaCO_3$ homeostat

The calcite homeostat is negative feedback which balances the input and output of alkalinity to and from the ocean. The major inputs of alkalinity to the open ocean are river discharges of weathering products, and to a lesser degree those from hydrothermal vents. The output is only represented by $CaCO_3$ burial at the sea floor. Nowadays, the input of alkalinity is 0.13 $\mathrm{Pg\ C\ yr^{-1}}$, and the same amount is balanced by deep sea burial. Calcifying organisms use the alkalinity to build $CaCO_3$ structures which then suffer from water column and sediment dissolution, releasing back alkalinity (Sarmiento & Gruber, 2006) (Figure 1.11). When the input and output are not balanced, the $[CO_3^{-2}]$ together with calcium ion could either increase or decrease. Changing in the $[CO_3^{-2}]$ would lead to a shift in the $CaCO_3$ saturation horizon, and so in the quantity of $CaCO_3$ that gets buried. The negative feedback

brings to a deepening (shoaling) of the calcite saturation horizon when the input of alkalinity is higher (lower) than its output. The calcite saturation horizon continues to deepen or shoal until a new balance is reached. The time needed for the entire pool of DIC to change due to input from weathering processes and volcanic outgassing is on timescales of 100,000 years. However, being the $[CO_3^{-2}]$ only 5% of the total dissolved inorganic carbon, the time needed to fully adjust its concentration is ~5000 – 10,000 years (Sarmiento & Gruber, 2006). Since, on millennial timescales the deep ocean also controls the atmospheric $CO_{2(g)}$ concentrations, the calcite homeostat is considered important also in controlling the $CO_{2(g)}$ (Broecker, 2003; Sarmiento & Gruber, 2006; Zeebe, 2012).

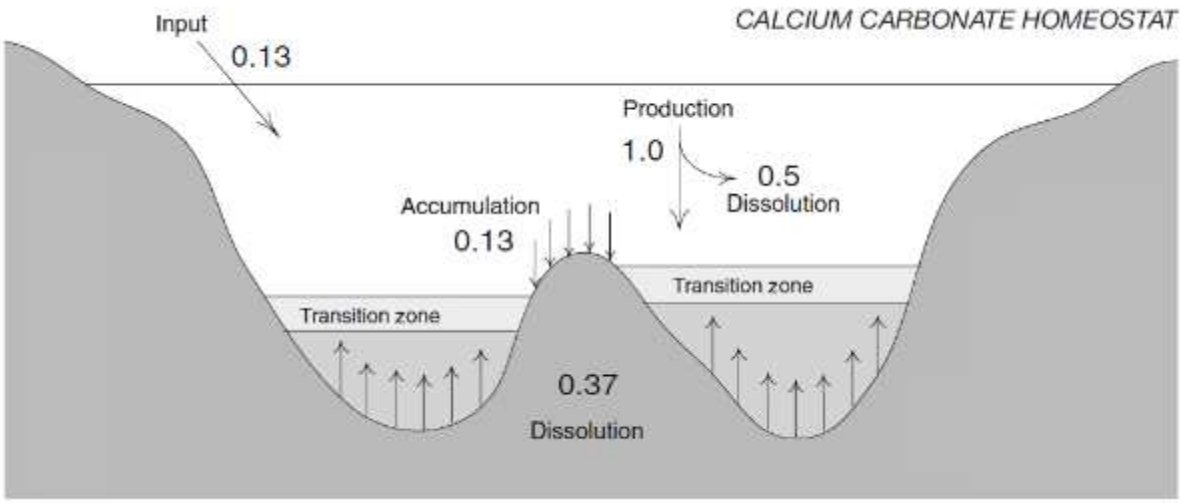

Figure 1.11| Illustration of the nowadays $CaCO_3$ homeostat. The values are in Pg C yr^{-1}. Picture modified from (Sarmiento & Gruber, 2006).

1.9 Glacial-interglacial cycles and possible implication with the carbonate system

Many theories have been proposed to explain the atmospheric CO_2 shift. Nowadays, one of the most debated theory concerns changes in the global ocean thermohaline circulation on millennium timescales (Sigman et al., 2010; Zhang et al., 2022). This hypothesis, called 'ventilation hypotheses' considers the reduction in the release of CO_2 from the upwelling system in the Southern Ocean, to be the cause of a decrease in atmospheric CO_2. Indeed, increased stratification and increased ice coverage during glacial periods would have decreased the water surface exposed to the atmosphere in the Southern Ocean (Sigman & Boyle, 2000). Moreover, due to a more efficient consume of the reduced nutrient supply from the Antarctic phytoplankton, there was a further CO_2 storage in deep waters. The Subantarctic Zone productivity was higher, contributing to the reduction of $[CO_2]$, before it could escape from the surface ocean to the atmosphere. At the same time, the NADW shoals, leaving the ocean floor mostly exposed to the slow ventilation of the low preformed nutrient concentration, high $[CO_2]$ Southern deep waters. In this theory, the carbonate homeostat mechanism has an important role. Indeed, the total decrease of 80 ppmv in the atmospheric CO_2 would not be possible if not also considering the carbonate compensation. Indeed, the negative feedback of the

carbonate system in response to the increased acidity of the deep ocean waters would have dissolved more $CaCO_3$ and released CO_3^{-2}, increasing the alkalinity, which in turns would improve the ability of the ocean to absorb CO_2 atm (Sigman et al., 2010).

1.10 Aim

The atmospheric CO_2 variations between G-IG are triggered by orbital changes, and the biological, physical, and chemical oceanic processes are the responsible for the carbon reorganization in the Earth system. It has been hypothesized that ocean stratification, and transport of dissolved inorganic carbon from intermediate to deep water, were the main factor which led to the decline in atmospheric CO_2 during glacial periods. The increased acidity of deep-water masses would have triggered dissolution of $CaCO_3$ and so increased oceanic ALK, which would get used to absorb more atmospheric CO_2. The assessment of $CaCO_3$ records all over the different Oceanic basins is an important tool to validate the existing hypothesis. The $CaCO_3$ weight in ocean sediments depends not only on dissolution and/or preservation, but also by biogenic productivity, and dilution which makes more difficult the direct interpretation of the results. In the middle way of the global thermohaline circulation is the Indian Ocean, which connects the Atlantic and Pacific Oceans, and features a medium saturation state of $CaCO_3$, due to the medium-aged deep waters.

This study aims at the reconstruction of the $CaCO_3$ record from sediments collected in the equatorial Indian Ocean, and to the identification of possible relationships with orbital cycles. To clarify the nature of the $CaCO_3$ fluctuations, the relationship with organic matter flux will be assessed and related to possible sediment dissolution, while the dilution effect will be also considered.

Chapter 2

STUDY AREA, MATERIAL AND METHODS

2.1. Study Area

Samples used in this study are from Site U1443, drilled during the International Ocean Discovery Program (IODP) Expedition 353 (29 November 2014 – 29 January 2015). The Site is located on the northern end of Ninetyeast Ridge in the southernmost Bay of Bengal (5°23.05' N, 90°21.67' E, water depth 2,924 m) (Clemens et al., 2016a) (Figure 2.1).

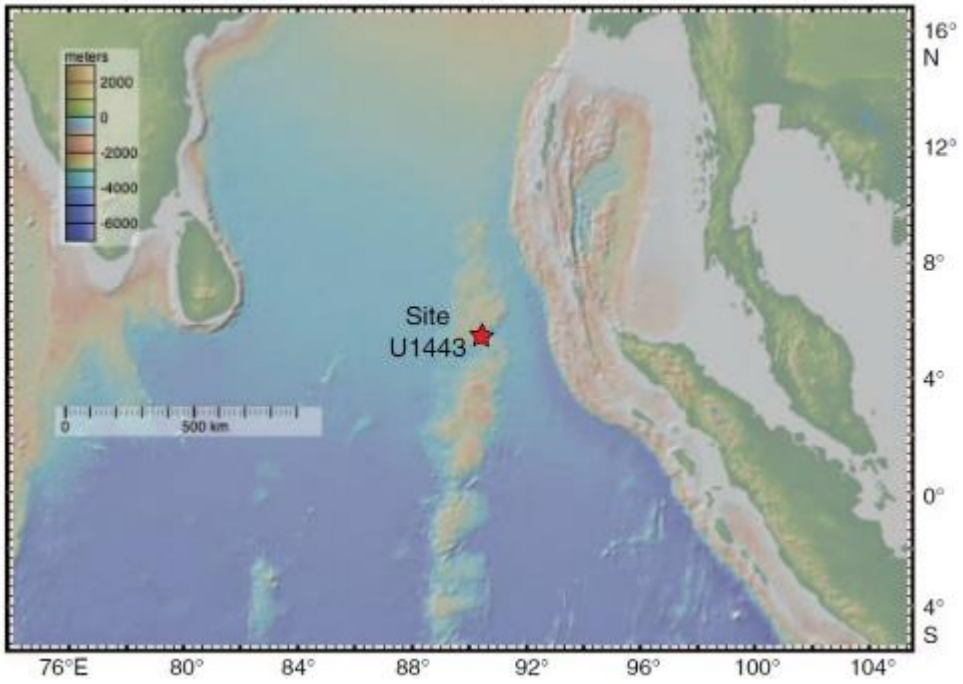

Figure 2.1| Bay of Bengal bathymetric map with the Site U1443 of the International Ocean Discovery Program (IODP), Expedition 353. Modified from (Clemens et al., 2016a).

IODP Site U1443 is a redrill of Ocean Drilling Program (ODP) Site 758 (Clemens et al., 2016a), which has proven to be a high-quality palaeoceanographic archive, and it has been intensively investigated in the past (e.g., Misra and Froelich, 2012; Bolton et al., 2013; Ali et al., 2021), hence its material was heavily depleted.

2.1.2 Oceanographic and atmospheric setting

The surface oceanography of the northern Indian Ocean features strong seasonal changes tied to the Indian monsoons system (Clemens et al., 2016a; Cullen & Prell, 1984). The latter during the summer months June, July, and August (JJA) is characterized by an atmospheric pressure gradient between the Indo-Asian continent (low) and the southern subtropical Indian Ocean (high) (Clemens et al., 2016a). The southwesterly winds originated by these gradients carry moisture that is eventually released over the Bay of Bengal, South Asia, and Southeast China (Clemens et al., 2016a). During the winter months December, January, and February (DJF) wind stress originates in the opposite direction and trigger winter monsoons, but with lower strength than the summer monsoons. Site U1443 experiences seasonal changes in surface ocean currents, due to winds stress of monsoon system (Clemens et al., 2016a). During (JJA), the southwesterly winds give rise to a clockwise circulation, which lead to the southward flowing of the West Indian Coastal Current (WICC) (Clemens et al., 2016a). The latter connects with the Southwest Monsoon

Current (SMC), on the tip of India and Sri Lanka and both carry high salinity waters eastward into the Bay of Bengal (Clemens et al., 2016a). The southwesterly winds also trigger the East Indian Coastal Current (EICC) to flow northward, driving to an intense coastal upwelling (Clemens et al., 2016a). During the winter monsoon, the northeasterly winds drive surface circulation counterclockwise and in the opposite directions than the summer currents (Clemens et al., 2016a). Accordingly, depth of the surface mixed layer at the location of Site U1443 changes due to the influence of summer and winter monsoon winds. Indeed, in both seasons it is possible to notice a little increase in primary productivity due to the increase in depth of the surface mixed layer, which favors the injection of deep nutrients into the photic zone. More specifically with higher rate during summer monsoon than in winter (Bolton et al., 2022; Lübbers et al., 2019). The dominance of the summer precipitation signal is well reflected in the Bay of Bengal surface salinity patterns (Figure 2.2), which vary between 20 and 34 over seasonal and spatial scales and reach the lowest values in August and September (Clemens et al., 2016a). A total of 12 major rivers discharge monsoon-fueled freshwater into the Bay of Bengal, with a volume of 943×10^9 m^3 of freshwater in summer (Clemens et al., 2016a) that contributes to the development of the observed salinity gradient. Salinity in the southern Bay of Bengal, where IODP Site U1443 is located, is closely pinned to

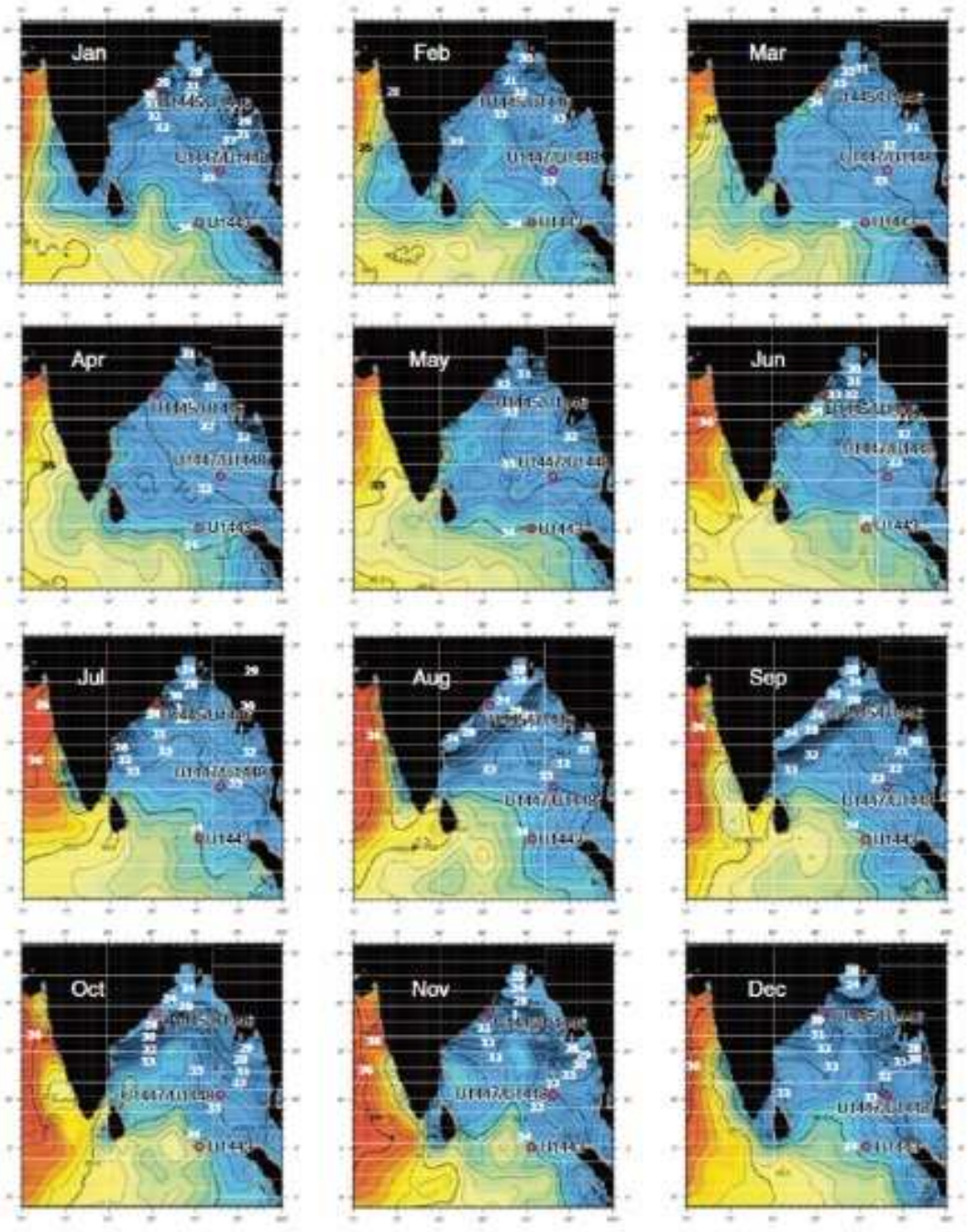

Figure 2.2| Monthly Salinity for 1955-2006 (Antonov et al. 2010). Areas drilled in the Adman Sea, Mahanadi basin, northern Bay of Bengal, and Ninetyeast Ridge, modified from (Clemens et al.2016).

the 34 isohaline year round without significant seasonal variability (Clemens et al., 2016a). During the summer monsoon season, terrigenous material delivered from river discharges slightly influences Site U1443 particles flux, while during the rest of the year, Site U1443 features typical low open ocean input of terrigenous material. On Site U1443 the absence of high fluctuations in environmental features, which instead are typical of non-open ocean sites in the Bay of Bengal, allows to better isolate possible global response in $CaCO_3$ % fluctuations over G-IG cycles. Intermediate and deep water masses in the Indian Ocean originate from the Atlantic and Southern Oceans (Kawagata et al., 2006) (Figure 2.3).

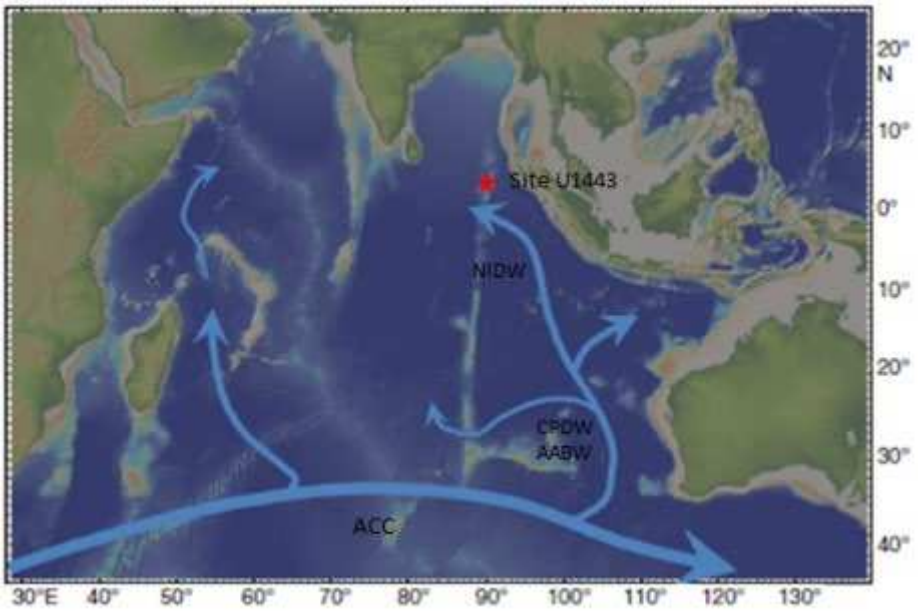

Figure 2.3| Indian Ocean deep water circulation. With the representation of the antarctic circumpolar current (ACC), antarctic bottom water (AABW), circumpolar intermediate water (CPIW), and north indian deep water (NIDW), picture modified from (Clemens et al., 2016a).

Abyssal depths of >3800m are bathed in cold, well-oxidized Antarctic Bottom Water AABW ($[co_3^{-2}]$~ 80 µmol/kg) (Kawagata et al., 2006). Depths between ~1200 and ~3800 m, above AABW, are bathed by North Indian Deep Water (NIDW). In the eastern Indian Ocean, NIDW originates from Circumpolar Deep Water (CPDW), which is admixed with NADW (Temperature 2°C, salinity 35.85 psu, oxygen 4.7 ml/l, $[co_3^{-2}]$~120 µmol/kg). North Indian High Salinity Intermediate Water (NIHSIW) are present in the upper ~1000 m of the Bay of Bengal (Kawagata et al., 2006).

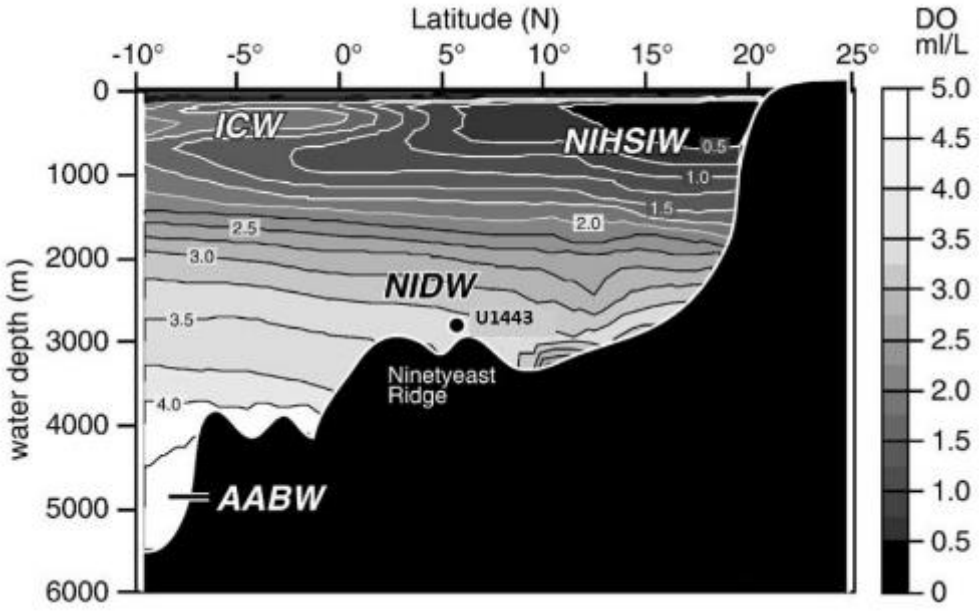

Figure 2.4| Vertical profile of dissolved oxygene content along 5˚N (NER), which help to identify the different water masses. The Site U1443 on the NER is exposed to NIDW, modified from (Kawagata et al., 2006).

The Site U1443 (reperforation of the ODP 758) is bathed by the lower part of eastern NIDW ($[co_3^{-2}]$~ 80 μmol/kg) (Kawagata et al., 2006) (Figure 2.4).

2.1.3 Calcium carbonate system features

The present-day lysocline on the Ninetyeast Ridge is positioned at a depth of 3,800 mbsl (Cullen & Prell, 1984), and the present day CSD in the Central Indian basin is close to 3200 m depth (Zhang et al., 2022). The greatest depth reached by the lysocline, during the last 500,000 years has been of 2,800 m (Bassinot et al., 1994). The lysocline shoals to the position of the Site U1443 in the interglacial between 500-300 ka (Peterson & Prell, 1985). The CSD shoals from southern to the northern Indian Ocean, mirroring the increase ventilation age of northward inflow of deep water mass (Zhang et al., 2022). The CCD is close to 4600 m among all different Indian Basins (Zhang et al., 2022), and has remained between 4.0 ± 0.6 km over the last 65 Ma (Broecker, 2008). Site U1443 is therefore considered well situated to record the possible deep water carbonate ion fluctuations that gave rise to the CSD and lysocline systematic changes between glacial and interglacial periods (Peterson & Prell, 1984; Zhang et al., 2022).

2.1.4 Geological setting

The Ninetyeast Ridge is a north-south oriented, aseismic volcanic ridge which is located in the central part of the Indian Ocean between ~10°N and ~31°S. It is

named after its position parallel (and close) to the 90°E Meridian (Weissel, 1991). It formed by age-progressive hotspot volcanism from plume sources, which is currently positioned beneath the Kerguelen Plateau (Clemens et al., 2016a). As a result of the Indo-Australian tectonic plate drift northward, IODP Site U1443 moved from temperate southern latitudes to ~5°S during the Late Cretaceous (Campanian ~ 83 – 72 Ma), and reached its present location at ~5°N during the past 35 Ma (Clemens et al., 2016a, 2016b). The Bay of Bengal seafloor features a large submarine fan system, the Bengal Fan. Its development started during the Early Eocene and was associated with the uplift and denudation of the Himalaya, which caused a large sediment load to be discharged into the Bay of Bengal by the Ganges-Brahmaputra River system (Cullen & Prell, 1984). Ever since, the sediment types and fluxes delivered through river discharge into the Bay of Bengal are controlled by weathering regimes, tectonic activity, and climate change in the Himalayan sediment source (Bahk et al., 2019). The Ninetyeast ridge top rises to ~3,500m above the surrounding abyssal plain and features depths as shallow as ~2,000 meters below sea level (mbsl). The top ridge position of the Site U1443 is not significantly affected by the sediments inputs associated with the Bengal Fan (Clemens et al., 2016a), which instead mainly affect the sediment composition of the abyssal plane. Therefore,

these characteristics makes the Site U1443 an ideal location for the recovery of continuous, open ocean, pelagic sedimentary records (Clemens et al., 2016a).

2.1.4.1 Indian Ocean background

The Quaternary $CaCO_3$ cycles into the sediments of the Indian Ocean are overall more sparsely documented than in the Atlantic and Pacific Oceans. During the Quaternary glacial and interglacial cycles, the calcium carbonate concentrations fluctuated in different ways between Atlantic, Pacific, and Indian Ocean. It is widely accepted that in the Atlantic Ocean the calcium carbonate records show lower percentages due to higher dissolution during glacial periods and higher percentages and preservation during interglacial, while in the Pacific Ocean the opposite is true (Divakar Naidu & Malmgren, 1999). Some studies show the presence of both "Pacific and Atlantic carbonate patterns" in the Indian Ocean (Bassinot et al., 1994; Divakar Naidu et al., 1993; Farrell & Janecek, 1991; Peterson & Prell, 1985), while others exhibit only "the Pacific pattern" (Naidu, 1991; Tadamichi, 1969). Available data indicate that equatorial Indian Ocean cores that are marked by greater dissolution (Peterson & Prell, 1984; Tadamichi, 1969) generally exhibit a Pacific type of dissolution pattern (Divakar Naidu & Malmgren, 1999). The presence of many different basins in the Indian Ocean complicates the reconstruction of a shared regional record. Moreover, most of them are affected by strong terrigenous dilution

as the case of the Arabian Sea, which $CaCO_3$ record is mostly influenced by terrigenous dilution, variations in the summer monsoon intensity, and/or magnitude of the particulate sediment load discharged by the regional rivers (Naidu, 1991). Divakar Naidu & Malmgren, (1999) have conducted analysis on the Indian Ocean sediments, whereas neither dissolution nor dilution have effect on the $CaCO_3$ sediment content. They analyze the relationship between pelagic calcium carbon productivity and $CaCO_3$[wt. %] sediment content on G-IG cycles. In this study they verified the absence of any correlation between $CaCO_3$ sediment content from above the lysocline and G-IG cycles, while showing the presence of strong correlation with biological calcium carbonate productivity. Likewise, Yadav et al., (2022) have found a strong relationship between primary productivity in the uppermost water column and carbonate dissolution in sediments above the regional lysocline in the equatorial Indian Ocean. Other studies applied the use of dissolution proxy on sediments of the equatorial Indian Ocean (Bassinot et al., 1994; Divakar Naidu et al., 1993; Farrell & Janecek, 1991; Peterson & Prell, 1984). The application of the Composite Coarse Fraction Index (CCFI) on sediments from the Ninetyeast ridge (Bassinot et al., 1994; Farrell & Janecek, 1991) covering the time span of the last 1500 kyr, evaluated the presence of major degree of dissolution during interglacial. The CCFI index seems to agree with the Composite Dissolution Index

(CDI) applied by Peterson & Prell, (1984), and with coarse fraction dissolution index (wt.%>150μm) applied by Farrell & Janecek, (1991) on sediments from the Ninetyeast Ridge. Hence, all of them (Bassinot et al., 1994; Farrell & Janecek, 1991; Peterson & Prell, 1984) show the presence of a 'Pacific Pattern' in the Indian Ocean. The ratio of 'dissolution susceptible' to 'resistant' planktic foraminifera species used by Divakar Naidu et al., (1993) in deep-sea cores from the tropical Indian Ocean at G-IG time scales also indicate that better preservation of calcium carbonate is present during glacial periods, and also that the main factor controlling the $CaCO_3$ cycles into the sediment is carbonate dissolution. However, most published records are qualitative and often suffer from complicating factors such as pore water dissolution and surface productivity changes (Broecker, 2008; Yu et al., 2013).

2.1.5 Core sediments features

This study focuses on the analysis of Unit I a of the Hole U1443B, specifically on sections 1H-1 through 1H-6, which span a time period of the last 460 ka (part of the middle Pleistocene, late Pleistocene and Holocene). Sediments recovered from the first ~100 m of the core drilled in the IODP Site U1443, consist of a range of pelagic and hemipelagic sediments. The dominant lithology is represented by clayey nannofossil ooze with foraminifera and a lower lithological fraction by

volcanic ash (Clemens et al., 2016b). The core sediments are characterized by a downhole decrease in both clay and volcanic ash content and a corresponding increase in calcareous nannofossil and authigenic carbonate content (Clemens et al., 2016a). A volcanic ash layer dominated by vitric grains with varying amounts of feldspar, quartz, and biotite is dominant on the core fraction stretching the first 69-88 cm, which prevented the collection of $CaCO_3$ samples (Clemens et al., 2016b). The Pliocene to Holocene tephra layers of the northern Ninetyeast Ridge provide a unique record of explosive volcanism derived from the Indonesian island of Sumatra, the northernmost part of the Sunda arc, and the nearest volcanically active region (Clemens et al., 2016a). Some thin bands with higher iron sulphide content occur, particularly between 0.5 and 9 m, and there is a persistent trace (<5%) contribution of biosilica, including radiolarian, sponge spicule, and silocoflagellate fragments, which decrease downhole (Clemens et al., 2016b). Nannofossil assemblages (Figure 2.5 A, B) are typically dominated by tropical to subtropical taxa and are well preserved in the Pleistocene to late Miocene sections, analysis revealed that *Emiliania huxleyi* (<0.29 Ma) is present in the first centimeters of the core (0–10 cm) (Clemens et al., 2016b). The good nannofossil preservation could result from the enhanced clay content of these sediments relative to deeper lithostratigraphic units. Indeed the clay-rich sediments have low porosity and

permeability, therefore carbonate fossils are sealed in with their associated pore water fluids, and rapid carbonate chemistry equilibration occurs (Clemens et al., 2016b). Pleistocene assemblages are typically tropical/subtropical and included abundant *Florisphaera profunda, Gephyrocapsa* spp., *Reticulofenestra* spp., *Sphenolithus* spp., *Discoaster* spp. *Helicosphaera* spp., *Calcidiscus* spp., and *Umbilicosphaera* spp. (Clemens et al., 2016b). Foraminiferal assemblages (Figure 2.5 C, D) are dominant and generally well preserved. Planktonic foraminifer percentage is >95%, and 250–700 benthic foraminifers are found in the >150 μm size fraction of the Pleistocene samples (Clemens et al., 2016b). Planktonic assemblages are dominated by the tropical and warm subtropical species *Pulleniatina obliquiculata, Neogloboquadrina dutertrei, Globoquadrina conglomerate, Globigerinoides ruber, G. sacculifer, Globigerinoides trilobus, Globorotalia menardii, and Orbulina universa* (Clemens et al., 2016b).

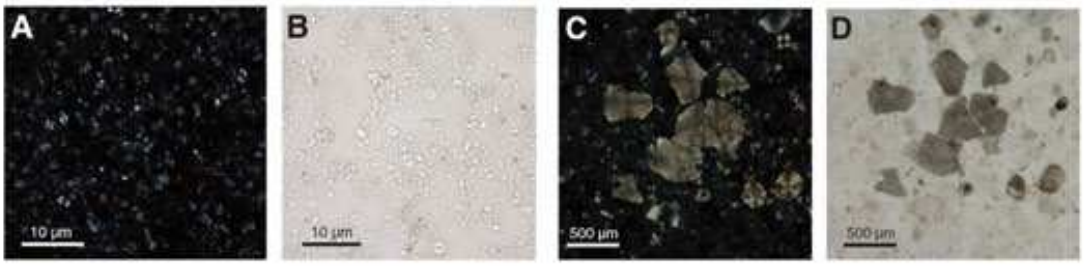

Figure 2.5| Main biogenic sedimentary components found in Site U1443 of the IODP 353. A: Nannofossils; B: Nannofossils including *Discoaster* spp.; C, and D: Large fragments of planktonic foraminifera, picture modified from (Clemens et al., 2016b).

The diatom assemblage in the uppermost 28 m of the Site U1443 is diverse and mainly consists of Pleistocene to Holocene species, mostly typical of warm to temperate low-latitude ocean waters (Clemens et al., 2016b). Valve preservation ranges from good to poor and tends to be better whenever abundance is higher. Warm-water species, including *Fragiliaropsis doliolus*, tend to dominate whenever total diatom abundance is higher than "few". Main contributors to the warm temperature group include: *Alveus marinus, Azpeitia nodulifera, F. doliolus, Rhizosolenia bergonii, Shionodiscus oestrupii, Thalassionema bacillaris, and Thalassiosira eccentrica* (Clemens et al., 2016b). Sporadic increases of diatoms at Site U1443 in downcore sediments are associated with the occurrence of volcanic glass shards. This phenomenon is related to the release of nutrients from the volcanic ash layers and represents the photo-physiological and biomass stimulation of phytoplankton communities following the supply of basaltic or rhyolitic volcanic ash (Clemens et al., 2016b). Other groups of microfossils such as silicoflagellates and radiolarians are also present, the former has a distribution similar to that of diatoms throughout the cores, whereas the latter can be common in levels completely barren of diatoms (Clemens et al., 2016b). Overall, the sediments have a high carbonate content (>80 wt.% throughout most of the section) and low total organic carbon (<0.3 wt.%) (Clemens et al., 2016a).

The mean sedimentation rate of the sampled sediments is of 1.20 cm kyr^{-1} (Clemens et al., 2016a).

2.2 Materials and Methods

2.2.1 Core drilling and sediment collection

During the International Ocean Discovery Program (IODP) Expedition 353 a total of six sites were drilled in the Bay of Bengal between November 29th, 2014 and January 29th, 2015 (Clemens et al., 2015). Site U1443, hole B (5°23.0190' N, 90°21.7091' E) was drilled on December 11th, 2014 using an advanced piston corer (APC) system (Clemens et al., 2015). A total of 40 cores have been collected from this hole, reaching a total depth below the sea floor (DSF) of 326.4 m. Data presented here have been generated from sediments taken from the core 1H that has a total length of 9 m, and covers the last 500 ka (Marino et al., unpublished data), and has been sampled at 1 cm resolution. Sediment samples used for this work range from section 1H-1 (50-51 cm) to section 1H-6 (35-36 cm), leading to a dataset that has high temporal resolution.

2.2.3 $CaCO_3$ measurements

For the inorganic carbon characterization, each sample has been freeze-dried, using the FreeZone Freeze Dryers for 48h. The freeze-drying process is necessary to

eliminate any trace of water from the sample, which would affect the inorganic carbon weight percent (% wt.) calculations targeted by this study. Moreover, freeze drying helps to disaggregate, homogenize, and grind the samples, more than other drying techniques (International Atomic Energy Agency, 2003). Indeed, during the freeze-drying process the ice crystals form within the sediments matrix and when they sublimate under vacuum, the left voids between grains easily collapse by shaking or gentle grinding. The core material was sampled, freeze-dried, and archived in 2015 by a team of collaborators at the Research School of Earth Sciences of the Australian National University and shipped to Palaeoclimatology Lab, GEOMA Group, Universiade de Vigo in October 2021. In humid environments dried samples may absorb humidity over time, thereby altering analysis based on weight percentage calculations. Comparison between the inorganic carbon percentages of the samples who have been freeze-dried again at the Universiade de Vigo and the inorganic carbon percentages of the same samples who have only undergone one freeze-drying procedure at the Australian National University shows that the latter have lowest $CaCO_3$ percentages. Marine sediment samples are rich in salt content, which is a highly hygroscopic substance. In the time span between 2014-2021, the highly hygroscopic samples, even if partially isolated from the external environment, have absorbed moisture that increases sample total weight. The highest total

weight of the old, freeze-dried samples determines the presence of a lower inorganic carbon percentage compared to the recently freeze-dried samples.

Prior to $CaCO_3$ determinations, freeze-dried samples are then ground, homogenized, and a quantity of ~ 10 mg is placed in a calibrated silver capsule. For calibration and weighing purposes, the Micro-Weighing Mettler Toledo scale of the Centro de Apoyo a la Investigación (CACTI) de la Universidade de Vigo was used to quantify the inorganic carbon percentage in the samples, we used the Gas chromatography-mass spectrometry (GC-MS) analytical method. The Carlo-Erba NA-1500 elemental analyzer uses the GC-MS to simultaneously determine total Carbon (C), Hydrogen (H), Nitrogen (N), Sulphur (S) in samples. Since the $CaCO_3$ quantities are calculated from the inorganic carbon %, and no distinction is made between inorganic and organic carbon in the GC-MS, all the samples after being weighted were calcined at 500°C for 4h to ensure the removal of all the organic carbon. The samples were subsequently analyzed in the gas-chromatograph. In the gas-chromatograph they undergo an instantaneous flash combustion, which vaporizes the samples into a gas phase. After that, the compounds are propelled by an inert gas, like helium, through the capillary column covered with a stationary phase substance. In the capillary column the different elements of a sample are divided due to their own volatility and polarity characteristics, which make them interact

differently with the stationary phase. After the passage through the capillary column, the samples are swept into the mass spectrometer at different time rates depending on their volatility and polarity. The mass spectrometer ionizes the different components and detects them due to the different electrical signal. The GC-MS produces many different peaks, which are time-related with the chemical-physical properties of the element and magnitude-related with the element concentrations. The inorganic carbon concentrations are then transformed into % for each sample and used to calculate the $CaCO_3$ % in each sample through the formula:

$$C\ \% * \left(\frac{100}{12}\right) = CaCO_3\ \%$$

which:

C % = *inorganic carbon percentage*

$CaCO_3$ % = *calcium carbonate percentage*

$\left(\frac{100}{12}\right)$ = *ratio between molar mass of* $CaCO_3$ *and molar mass of the C*

2.2.4 Revised size index

The application of the 'Revised Broecker-Clak size index' (REF) was assessed on 12 different samples extracted from the core 1H site U1443, hole B. The samples from the section 1H-4 (centimeters 39-40; 41-42; 45-46; 47-48; 78-79; 115-116;

117-118; 121-122) and those of section 1H5 (centimeters 3-4; 4-5; 5-6; 7-8). Samples for the revised size index measurement were chosen after considering the $CaCO_3$ % results, between those that showed higher or lower peaks of $CaCO_3$ %. Quantity of ~ 0.5 g bulk sediment was weighted and wet sieved through a series of sieves (mesh of 63 μm and 20 μm), and then separated into three size fractions (>63 μm, 63 to 20 μm, and <20 μm). Between different sieving procedures the sieves were cleaned using an ultrasonic bath (~3 h at 40 hrz), to remove any particle that was potentially trapped into the sieve mesh. All the fractions were exposed to 14,000 rpm centrifuge cycles (1h was enough to collect suspend particles from the two major fractions while 3h cycles were necessary for the <20 μm fraction), oven dried and weighed. For the wet sieving, the solution utilized was prepared with ultrapure water and Ammonia 5% (100 μL in 1 L), to reach the pH value ~ 8. From all the fractions the $CaCO_3$ content was measured with the Carlo-Erba NA-1500 elemental analyzer. The 'Index' was empirically calculated considering the $CaCO_3$ content of the different fractions:

$$\frac{(> 63\ \mu m + 63\ to\ 20\ \mu m)}{< 20\ \mu m + > 63\ \mu m + 63\ to\ 20\ \mu m}$$

The >63 μm, and 63 to 20 μm fractions contain foraminifera, and their fragments while the fraction <20 μm mostly contain coccolithophores. Entire foraminifera shells and their fragments dissolve at a comparable rate, while coccolithophores are way more resistant to dissolution than foraminifera. It means that the increase in dissolution will result in a decrease of the revised size index value.

2.2.5 Chronology and supplementary data from IODP Site U1443

The data of $CaCO_3$[wt. %] and the revised size index were plotted and analysed together with other existing data from the IODP Site U1443 hole B. Data were plotted using the age model and the sedimentation rate calculations (Marino et al., unpublieshed data) obtained by tuning with the chronology of nearby Ocean Drilling Program (ODP) Site 978 and developed by (Bolton et al., 2013). Chronology for ODP Site 978 through the last 500 Ka (Bolton et al., 2013) was obtained by tying their benthic foraminiferal stable oxygen isotopes ($\delta^{18}O$) to the global benthic $\delta^{18}O$ stack (Lisiecki & Raymo, 2005). Marino et al., unpublished data of $\delta^{18}O$ isotopes of *Neogloboquadrina dutertrei, Globigerinoides ruber and Trilobatus trilobus* are used as proxy of temperature. Moreover, Site U1443 has available data of X-ray fluorescence (XRF) element counts of calcium (Ca), barium (Ba), titanium (Ti) and iron (Fe). XRF elemental counts were used in this work as a proxy of relative terrigenous input and $CaCO_3$ biogenic productivity and relative

terrigenous input and organic carbon export, respectively. The use of elemental counts ratios is usually based on the differential mobilization of elements involved in physical or chemical weathering (Gebregiorgis et al., 2020). The paleo-productivity and organic export flux variations can be assessed considering the log (Ba/Ti). Total Ba in deep marine sedimentary environments, do not contain terrigenous Ba sources and matches with the biogenic Ba, whereas the terrigenous input is minimal as in the Site U1443 (Lübbers et al., 2019). Hence, is a useful indicator of productivity when normalized against the relatively constant clay flux in an open ocean site as in our case. Proxies obtained by XRF elemental counts ratios should be reported in logarithms scale to avoid any complication due to the ratio's property of asymmetry. Indeed, conclusions based on evaluation of the ratio between two elements (a/b), are not equivalent to (b/a), and since no rule suggest which element should stay at the numerator or denominator the use of log-ratios solve the problem (Aitchison, 1982; Weltje & Tjallingii, 2008). The composite proxy log (Ca/Terr), where Terr indicates the sum of the Ti and Fe, is an indicator of the relative contribution of carbonate and clay to the sediments (Lübbers et al., 2019). The use of the elements Fe and Ti relies on the assumption that both elements in marine sediments are directly linked to fluvial and/or eolian transport processes, due to their siliciclastic nature (Gebregiorgis et al., 2020).

2.2.6 Statistical analysis

The possible correlation and dependence between the different XRF proxies, the revised size index, the sedimentation rate, and the records of $CaCO_3$ in the sediments, and isotope records were assessed by statistical analysis run with the Statistical toolbox in MATLAB. All the records were first analyzed using the "rmoutliers" function in the Statistical toolbox MATLAB, to detect and eliminate outliers. Pearson and Spearman correlations were used to understand if data were linearly or monotonically correlated (Pearson, 1896; Spearman, 1961). In cases of significant response to the Pearson test (Pearson, 1896), the records were considered linearly correlated, while in case of significant correlation with Spearman test the records were considered monotonically correlated. In case of significative correlation, the function "stepwiselm" in the Statistical toolbox MATLAB was used to find the best fitting regression model.

2.2.5 Complementary data to Site U1443

Site U1443 is a redrill of the Leg 121 Site 758, which has available data of $CaCO_3$ wt.% bulk, and wt.% >150μm fractions, over the last 500 Ka (Farrell & Janecek, 1991). The $CaCO_3$ wt. % of >150μm fraction, is generally considered an index of $CaCO_3$ dissolution (W. H. Berger, 1982). The wt% >150μm fraction which contains entire foraminifera shells, would decrease due to the dissolution-induced

fragmentation. The revised size index trend from Site U1443, will be compared with the wt.% >150 μm fraction of Site 758.

Chapter 3

RESULTS

3.1 $CaCO_3$ wt.% record

Data for $CaCO_3$ (wt.%) are plotted *versus* age in Figure 3.1. $CaCO_3$ in this core is generally the main sedimentary component and accounts for an average of ~60 wt.%. This leaves at most a 40% (wt.%) composition to the terrigenous material, given that the biogenic silica abundance in Pleistocene sediments at this location is negligible (Clemens et al., 2015). The lowest $CaCO_3$ values of ~12% are related to volcanic ash horizons at ~75 ka, correspondent to the Toba ash layer (Clemens et al., 2016a). The record in the interval ~433-400 ka is characterized by a long prolonged $CaCO_3$ decrease with values going from 64% to 49%. From ~400 ka the record shows an apparent recurring patern with peaks of maximum $CaCO_3$ every ~11 Ka (Figure 3.1). The $CaCO_3$ values in the interval 342-283 ka oscillate around the mean (~60%) with a amplitude of ~20 wt.%. An evident negative peak of 48 wt.% at ~274 ka interrumpts the ~11,000 year-spaced oscillations. In the interval between ~267-101 ka some of these oscillations are less evident to give an apparent recurrence of ~22,000 years (i.e., one peak is skipped or muted). In the middle of the record at 253 ka, there is an isolate value of 76 wt%, which is also the higest of the record and is most likely an outlier.

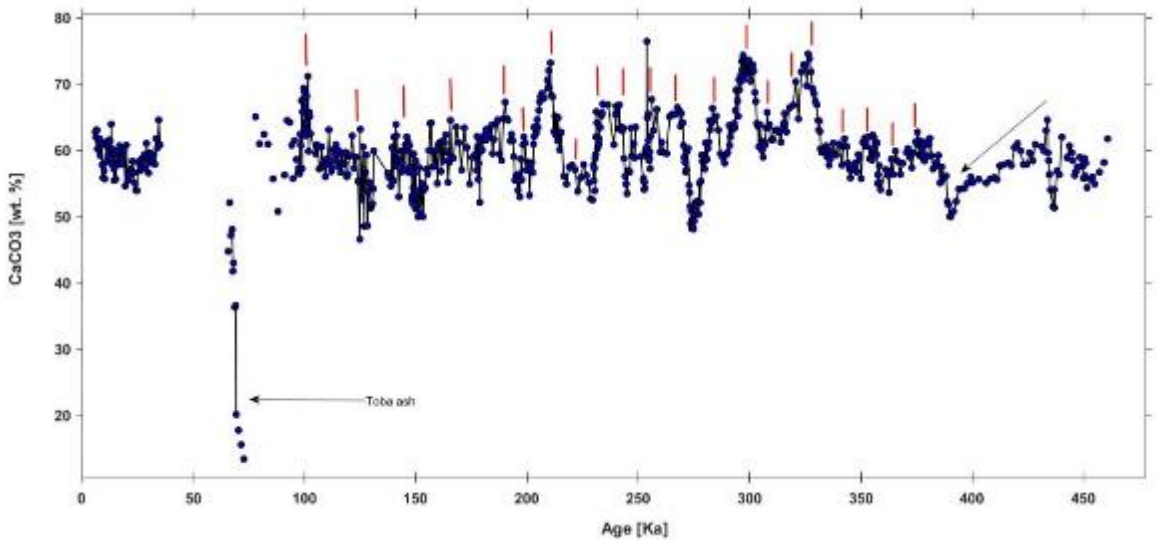

Figure 3.1| $CaCO_3$ [wt. %] bulk record from the IODP hole U1443B vs age. The black arrow show the prolonged declining period of $CaCO_3$ [wt. %]. The red lines highlight the positive peaks which oscillates with a time periodicity of ~11ka, and ~22ka (in the text).

3.2 Revised size index

The revised size index, with $CaCO_3$ (wt. %, calculated, and bulk) results are plotted together *versus* age in Figure 3.2. The $CaCO_3$ (wt. %, calculated), is empirically calculated from the sum of the $CaCO_3$ contents of all the different fractions of the revised size index (< 20μm; between 20 - 63 μm; > 63 μm). The revised size index values range from 0.73 to 0.94, while the $CaCO_3$ (wt. %, calculated, and bulk) values range from 48 wt.% to 74 wt.%. In the intervals 274-270, 304-300 ka, the index shows the presence of dissolution trends. Meanwhile, the values of $CaCO_3$ [wt. %] (calculated, and bulk) shows increasing values. The four samples in the

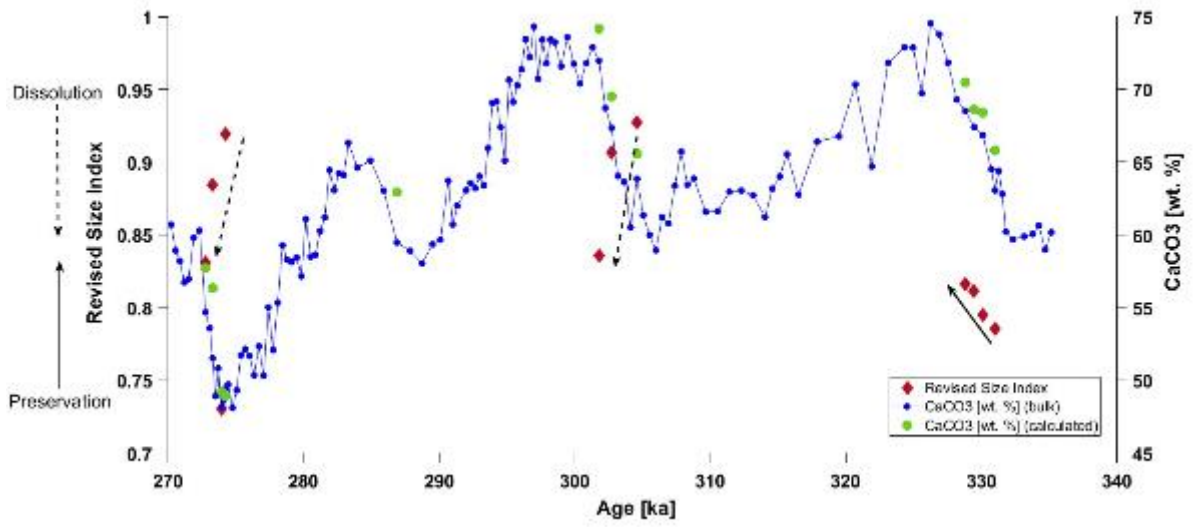

Figure 3.2| In the picture, the revised size index (red diamonds) on the left axis. On the right axis there is the calcium carbonate wt.%. The $CaCO_3$ [wt. %] calculated from the bulk (blue), the $CaCO_3$ [wt. %] empirically calculated from the sum of the $CaCO_3$ [wt. %] from the different fractions of the index, < 20 μm, and > 20 μm (green). The above values are plotted vs age in the interval anlyzed, 340-270 ka. The arrows in the graph are indicators of preservation (black full line), and dissolution (black dot line).

interval 274-270 ka, in order, has values of Age: (274.2, 273.9, 273.2, 272), revised size index: (0.91,0.73,0.88,0.83). The sample at 273.9 ka does not follow the dissolution trend of the interval 274-270 ka. The contribution to the total dry weight of the < 20 μm size fraction, for the sample at 273.9 ka has shown to be suspiciously high (31% of the total dry weight). For the same fraction (< 20 μm), the contribution to the total dry weight of all the other samples analyzed range

always below the 20%. Hence, the value of the sample at 273.9 ka, might be the result of artifacts associated with the sieving process. In the interval between 330-328 ka, the four samples analyzed show increasing values of revised size index, hence a preservation trend. For the same samples, the $CaCO_3$ [wt. %] (calculated, and bulk), have increasing values. The correlation between the bulk $CaCO_3$ [wt. %] and the $CaCO_3$ [wt. %] calculated by the sum of the concentrations in the different fractions are positively correlated (r =0.99; $p \leq 0.01$) (Figure 3.4). Hence, no material was lost by the different fractions (<20 μm; 20 < x < 63 μm; > 63 μm) during the sieving process.

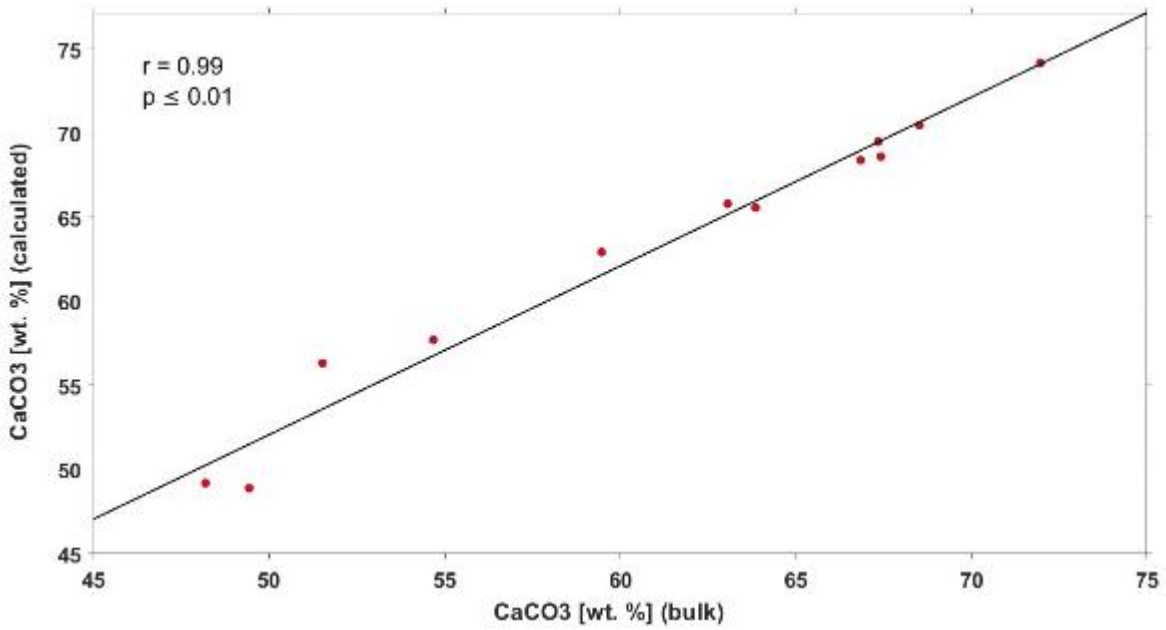

Figure 3.3| Cross correlation between the $CaCO_3$ [wt. %] calculated from sum of the different size fractions of the revised size index, and the $CaCO_3$ [wt. %] of the bulk. The Pearson correlation coefficient is 0.99.

3.3 X-ray fluorescence

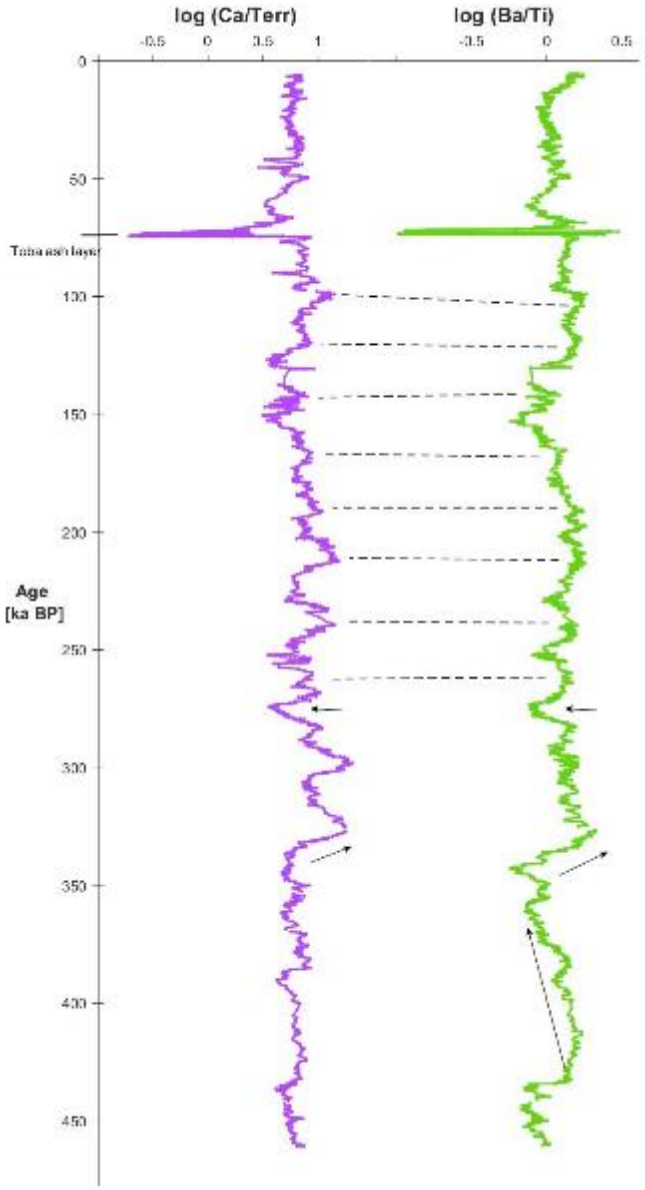

Figure 3.4| In the picture the log (Ca/Terr) (violet), and log (Ba/Ti) (green) plotted against age (ka). The dotted black line highlight the most evident correlated peaks between the two records. The black arrows evidentiates the negative peaks at 274 ka in both records, and the positive peak at 300 ka. At the interval 450-360 ka, the black arrow in the record log (Ba/Terr) evidentiates the long period decline in this experienced by this proxy.

The XRF log(Ba/Ti), and log(Ca/Terr) are from Marino et al. (unpublished data) and are plotted against age in Figure 3.4. Log (Ca/Terr) shows values fluctuation of -0.75, while log (Ba/Ti) has a lower magnitude fluctuation (-0.50). Between ~460 and ~350 ka, both records show an initial slight decrease, followed by the sharp increase of log (Ba/Ti) with an amplitude of ~0.36. Meanwhile, the log (Ca/Terr) keep low the values of relative biogenic export rate. From ~340 ka, both proxies show a steep increas of the values culminating in evident positive peaks at ~327 ka. In the middle core interval 268-101 ka, by visual analysis, both proxies shows oscillations with a periodicity of ~22 ka. Moreover, in both records there is an evident negative peak at 274 ka. The record of log (Ba/Ti) oscillates coherently with the log (Ca/Terr) values but with less magnitude at the positive peak at ~300 ka. Both records slightly declines between 200 to 150 ka, and increases between 150 to 100 ka. The Toba ash layer is evident as a negative peak between 76 an 65 ka in both proxies.

3.4 Isotope records of $\delta^{18}O$

Records of $\delta^{18}O$ of Site U1443 (Marino et al., unpublished data) are plotted *versus* age in Figure 3.5. The $\delta^{18}O$ records are plotted together with the LR04 global benthic $\delta^{18}O$ stack (Lisiecki & Raymo, 2005).

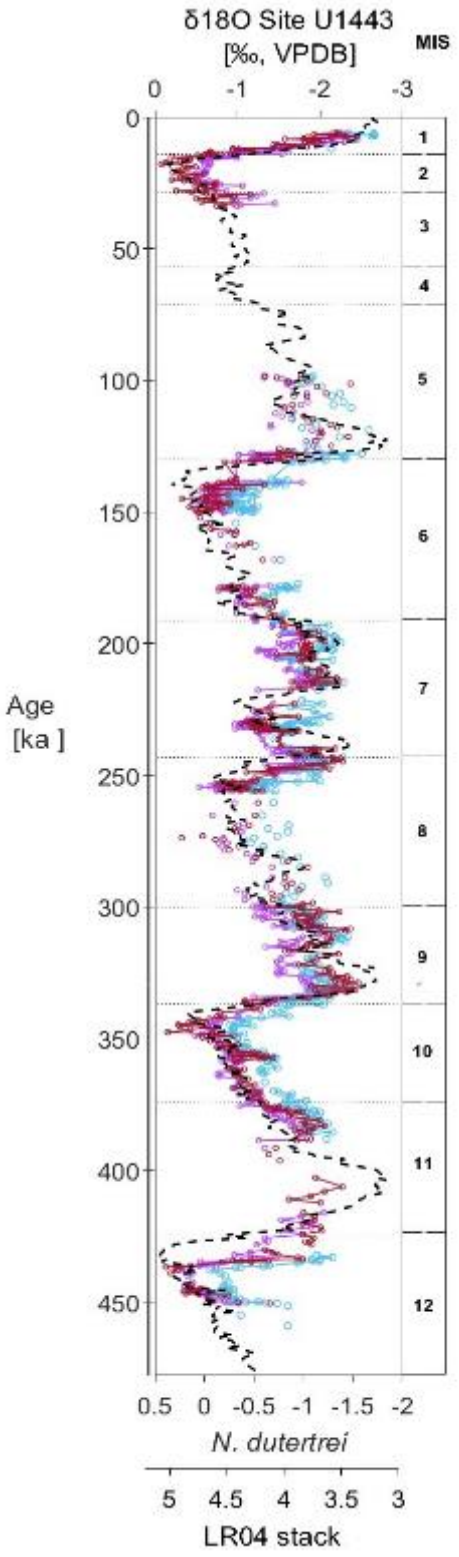

Figure 3.5| Site U1443 isotopic records of $\delta^{18}O$ of *T. trilobus* (purple), *G. ruber* (light blue), and *N. dutertrei* (red), plotted vs age. The benthic $\delta^{18}O$ of stack LR04 (black dotted line) is plotted together with $\delta^{18}O$ records of SiteU1443. The marine isotopic stages from Lisiecki & Raymo, (2005) are on the right column.

The Site U1443 $\delta^{18}O$ records show more negative values than those reported in the LR04 stack. Beside this difference, the $\delta^{18}O$ records of Site U1443 is highly coherent with the LR04 stack, allowing to identify the marine isotopic stages (MIS) defined by Lisieky and Raymo (2005). Shift of the $\delta^{18}O$ to more negative values indicate warm, less glaciated intervals, hence interglacial periods, while shifts towards less negative or positive values indicate colder, more glaciated intervals, hence glacial periods. The amplitude of the glacial-interglacial (G-IG) ~ 100 ka cycles of *N. dutertrei, G. ruber, and T. trilobus* $\delta^{18}O$ is ~1.18 ‰.

3.5 Sedimentation rate

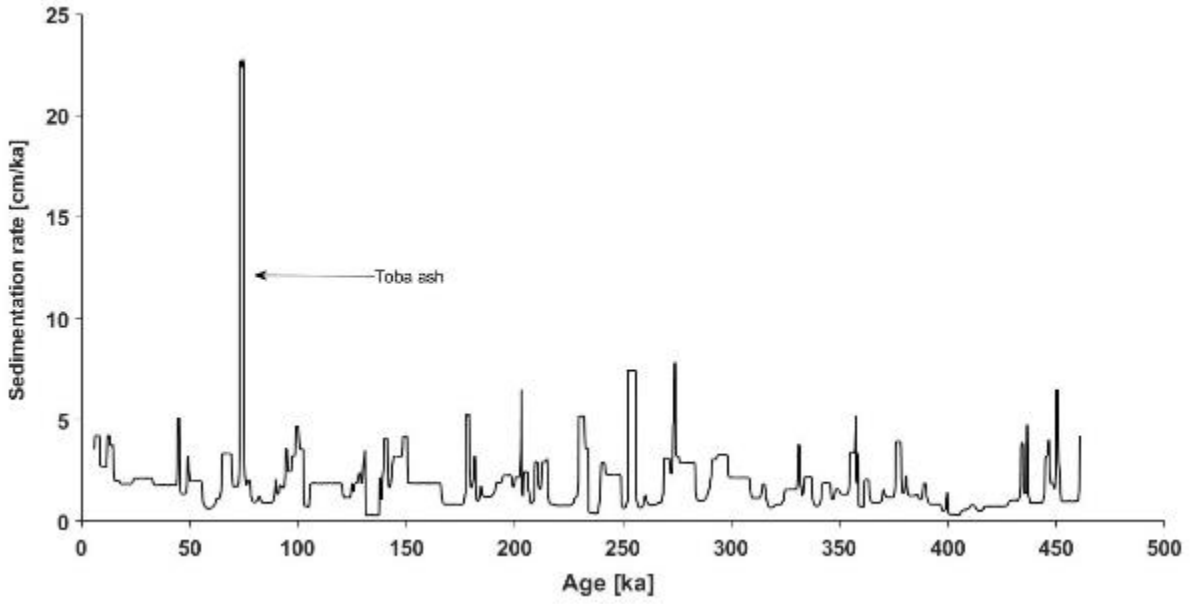

Figure 3.6| Sedimentation rate of IODP Hole U1443B. Toba eruption at 75 ka is highlighted.

The sedimentation rate is plotted *versus* age in Figure 3.6. It ranges from 0.1 to 0.8 cm/ka, excluding the 23 cm/ka coincident with the Toba eruption at ~75 ka (Clemens et al., 2016a). Lower values are recorded in the intervals 431-370, 346-298, 170-105 ka, which are interglacial periods. The highest peaks in the sedimentation rate occur in the intervals 460-430, 300-243 ka which corresponds to glacial period.

Chapter 4

DISCUSSION

The results of the analyses performed in IODP Site U1443 show interesting $CaCO_3$ wt.% fluctuations that can be put in the context of the reagional paleoceanographic changes through the last 460 ka. In the following paragraph, it will be illustrated and discussed, the relationship of the $CaCO_3$ fluctuations in deep-sea sediments from the equatorial Indian Ocean, with the contemporanoues changes in surface ocean primary productivity, dilution by terrigenous material, and dissolution.

Primary productivity, dilution, and dissolution have affected the $CaCO_3$ concentration at a different extent over the past 460 ka. Site U1443 is a redrill of Site 758, which data of $CaCO_3$ wt.% from Farrell & Janecek, (1991) are used for comparisons with the results of the analyses performed in this thesis. Mainly for what concerns the effect of dissolution on core sediments U1443, it is necessary to discuss in greater detail the case of interglacial MIS 11. Indeed, lysocline depth has reached the Site U1443 depth only during MIS 11 (Bassinot et al., 1994; Farrell & Janecek, 1991; Peterson & Prell, 1985), hence, by defnition determining an evident effect of dissolution on the $CaCO_3$ wt.% content (Broecker, 2003; Sarmiento & Gruber, 2006; Zeebe, 2012). Moreover, the suitability of the revised

size index as dissolution proxy on sediments from above lysocline is critically discussed by comparing it with the fragmentation proxy analysed on sediments from Site 758, by Farrell & Janecek, (1991).

4.1. $CaCO_3$ record from Indian equatorial sediments in the interval 460-0 ka

The $CaCO_3$ wt.% records obtained from Site U1443 and Site 758, have different time resolutions with the first being sampled at an interval of ~1 ka, while the latter at a time interval of ~5 ka (Farrell & Janecek, 1991) (Figure 4.1). Considering the different temporal resolutions, which makes more evident smaller oscillations in the record from Site U1443, the two records show exactly the same trend. Both records has apparently lower average values of $CaCO_3$ wt. % during glacial periods (Figure 4.1) (Farrell & Janecek, 1991). Visual analyses of $CaCO_3$ wt.% record of Site U1443 shows fluctuation patterns at shorter timescales than the ~100 ka eccentricity frequency that characterize the G-IG shifts of the Middle-Late Pleistocene (after the so called Mid Pleistocene Revolution), which are not evident in the Site 758 (Maslin Mark & Ridgwell Andy, 2005). The results obtained from rank correlation between the $CaCO_3$ wt.%, and $\delta^{18}O$ records (indicative of orbital variations) from Site U1443 has shown that they do not significantly correlate (r_s = -0.30).

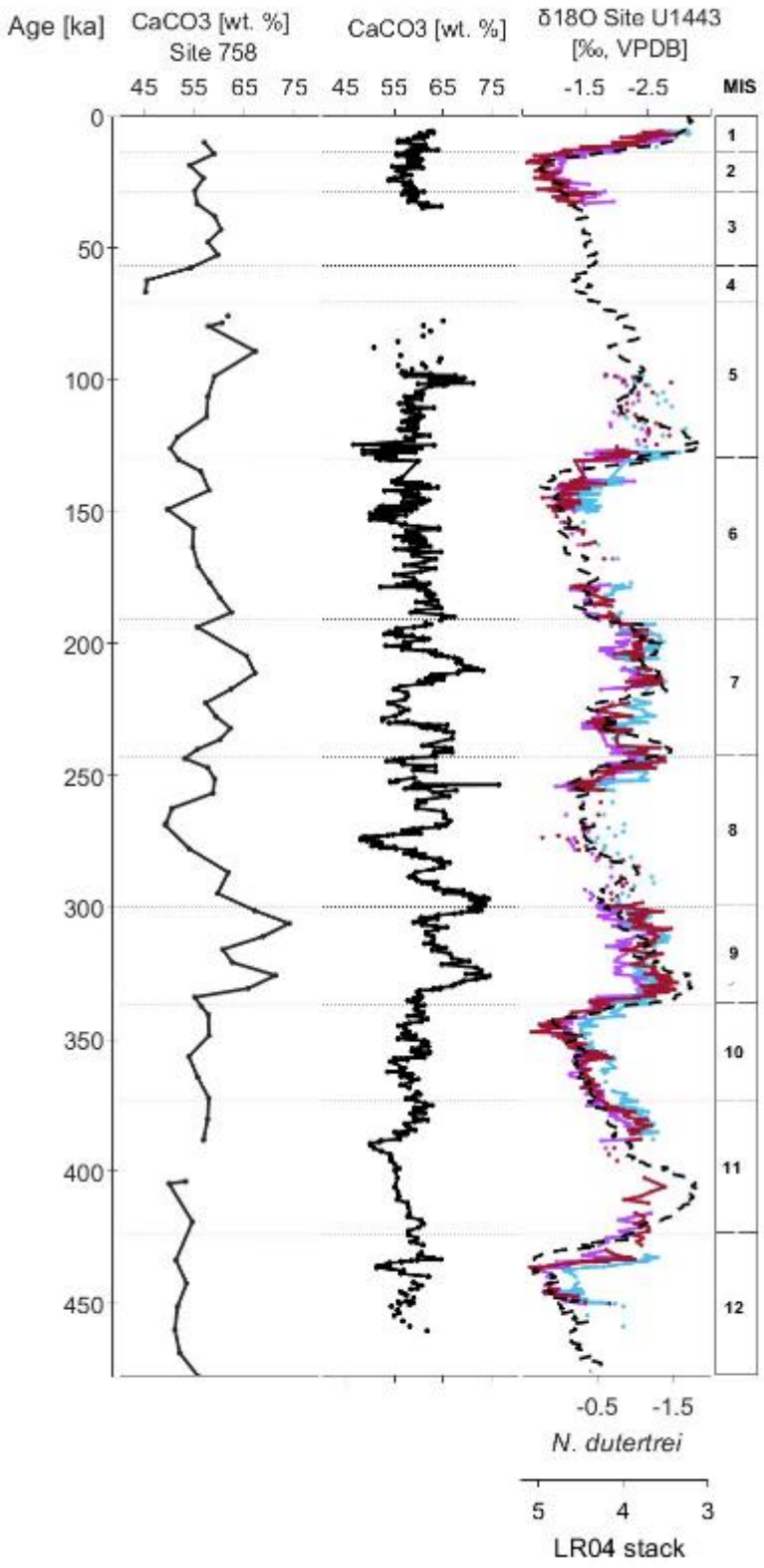

Figure 4.1| Plotted versus age, from the left: $CaCO_3$ [wt. %] records from Site 758 (Farrell & Janecek, 1991); $CaCO_3$ [wt. %] of Site U1443; records of $\delta^{18}O$ *T. trilobus* (purple), *G. ruber* (light blue), *N. dutertrei* (red), and stack LR04 (black dot line). The MIS from Lisiecki & Raymo, (2005) are indicated on the right column.

Therefore, suggesting that fluctuations in the $CaCO_3$ record are not in phase with G-IG periods (Figure 4.1). The $CaCO_3$ wt.% is considered to be a proxy for dissolution in marine sediments, due to its general decrease with water depth, but the relationship between the two is non-linear (Broecker, 2003). Because of the highly dependent of $CaCO_3$ wt.% from the initial export ratio of $CaCO_3$: $nonCaCO_3$ (terrigenous) material (Broecker, 2003). It is well known that dissolution, primary productivity and dilution by terrigenous materials control the final concentration of $CaCO_3$ in marine sediments (Broecker, 2003; Sarmiento & Gruber, 2006; Zeebe, 2012). However, the lack of evidence in $CaCO_3$ wt.% fluctuations between G-IG, at Site U1443, is not enough to declare the absence of a possible dissolution pattern caused by deep sea $[CO_3^{-2}]$ reorganization between G-IG (Broecker, 2003). Thus, because Site U1443 lies just above the modern and past lysocline depth (Bassinot et al., 1994; Farrell & Janecek, 1991), hence its sediments are only slightly affected by dissolution. The lysocline shoaled to the depth of Site U1443, only at the interglacial MIS 11 (Bassinot et al., 1994; Peterson & Prell, 1985), hence for most of the interval between MIS 10 to 1 dissolution did not have a great impact on the $CaCO_3$ [wt. %]. Moreover, the strong positive linear correlation between log (Ba/Ti), and log (Ca/Terr) ($p \leq 0.01$; r^2=0.66) suggests the 1:1 deposition ratio of C_{org}:C_{inorg}, therefore, the possibility of pore water dissolution can also

be discarded by the factors which mainly control the $CaCO_3$ [wt. %] fluctuations in Site U1443. Instead, the significant positive rank correlation between $CaCO_3$ [wt. %] with proxies of relative export of organic matter and $CaCO_3$($p \leq 0.01$; r_s = 0.44, r_s = 0.69), suggest that the $CaCO_3$ record of Site U1443 monotonically covary with primary productivity by $CaCO_3$-secreting organisms and dilution by terrigenous material during the last 460 ka. As understandable from these correlations, the terrigenous material makes the $CaCO_3$ wt.% decrease by dilution effect, while primary productivity increases. The effect of terrigenous dilution on the $CaCO_3$ wt.% record is highlighted by periods of high sedimentation rate related to low values of relative organic carbon and biogenic $CaCO_3$ export. Then, the export of organic matter, $CaCO_3$ and terrigenous material together control the final sedimentation rate; which has shown to have a significant positive Pearson correlation with $\delta^{18}O$ of *N. dutertrei,* and *G. ruber* ($p \leq 0.05$; $r^2 = 0.13, r^2 = 0.13$). Thus, the sedimentation rate is generally higher during glacial periods. In the marine isotopic stages (MIS) 6, 8, and 12, it is particularly evident how the increase in the sedimentation rate correlates with negative peaks in the $CaCO_3$ [wt. %], log (Ca/Terr), and log (Ba/Ti) records (Figure 4.2). Meaning, there is an effect of terrigenous dilution, in MIS 6, 8, and 12, which are cold and refer to low-stand sea levels.

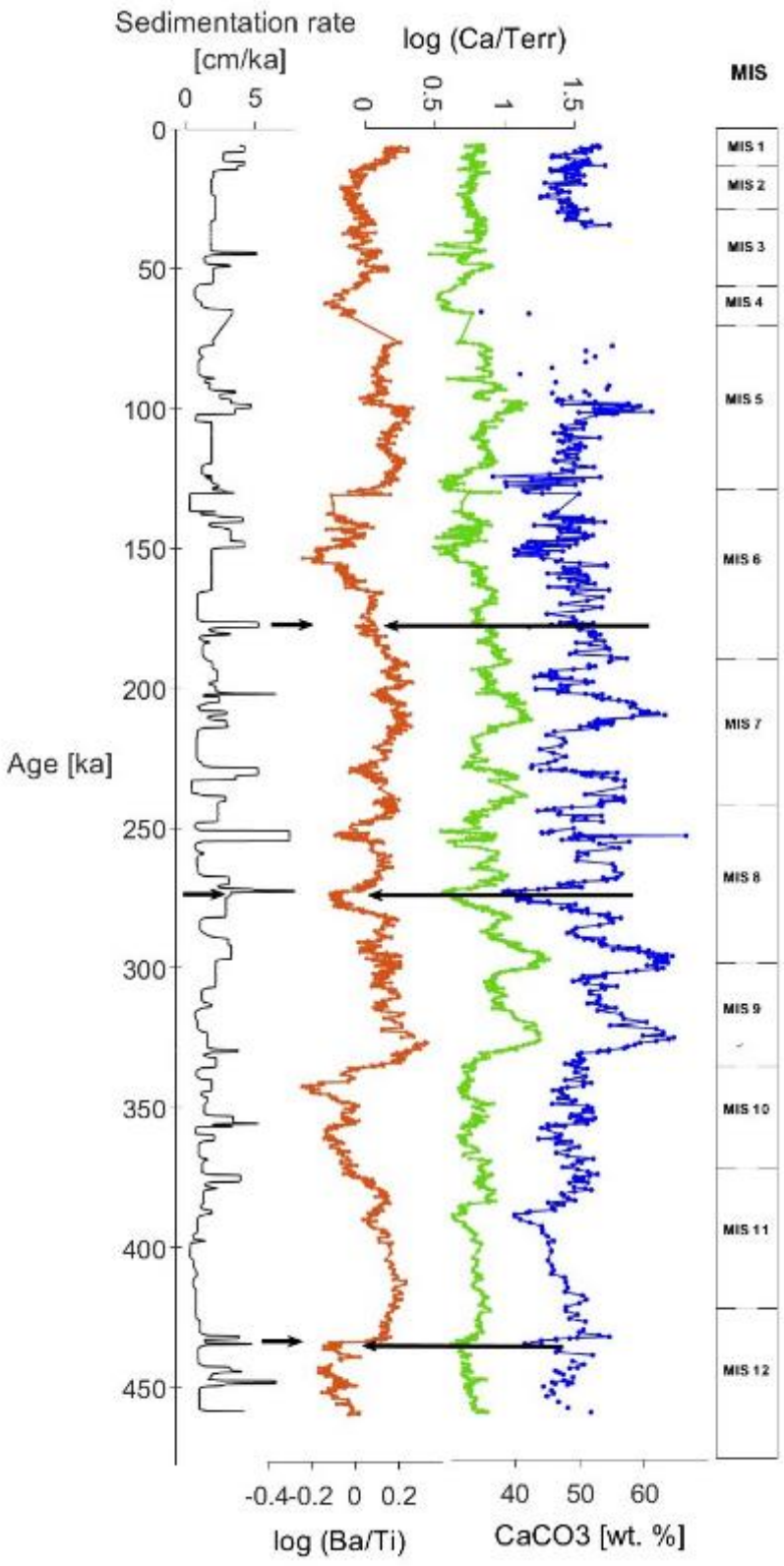

Figure 4.2| In the picture from the left, sedimentation rate (cm/ka) (black), log (Ba/Ti) (orange), log (Ca/Terr) (green), $CaCO_3$ (wt. %) (blue). On the right column the MIS identified by Lisiecki & Raymo, (2005).The terrigenous dilution during MIS 8, and 12 is indicated by the black arrows.

Curray et al., (1982) suggests that during glacial sea level low-stands, terrigenous sediments trapped on the continental shelf at the Ganges-Brahmaputra mouth, were eroded off the continental margin into the Bay of Bengal, and transported by turbiditic currents toward the Ninetyeast ridge. Accordingly, Farrell et al., (1991) in Site 758 also identified the presence of higher dilution effect by terrigenous material during glacial periods. Also, if the dilution effect increases during glacial periods, this is not always detectable in the $CaCO_3$ wt.% record of Site U1443. Indeed, in a wide portion of the record (Figure 4.2) the sedimentation rate coherently fluctuates with the records of $CaCO_3$ wt.%, log (Ba/Ti), and log (Ca/Terr). This suggests that important effects of dilution by terrigenous material do not affect the record. $CaCO_3$ wt. %, has been shown to fluctuate with a frequency of ~11 ka, and ~22 ka. The visual analyses of log (Ba/Ti), and log(Ca/Terr) also detected fluctuations with frequency of ~22 ka (Figure 4.3). As already observed in Site U1443, the terrigenous input material exerts a weak control on the $CaCO_3$ wt. % record, while dissolution barely affects the record. Hence, it is inferred that the $CaCO_3$ wt. % fluctuations reflect primary productivity. The primary productivity at the Site U1443 is seasonally controlled by changes in the surface-mixed layer thickness triggered by the Indian monsoon system activity (Bolton & Stoll, 2013; Clemens et al., 2016a).

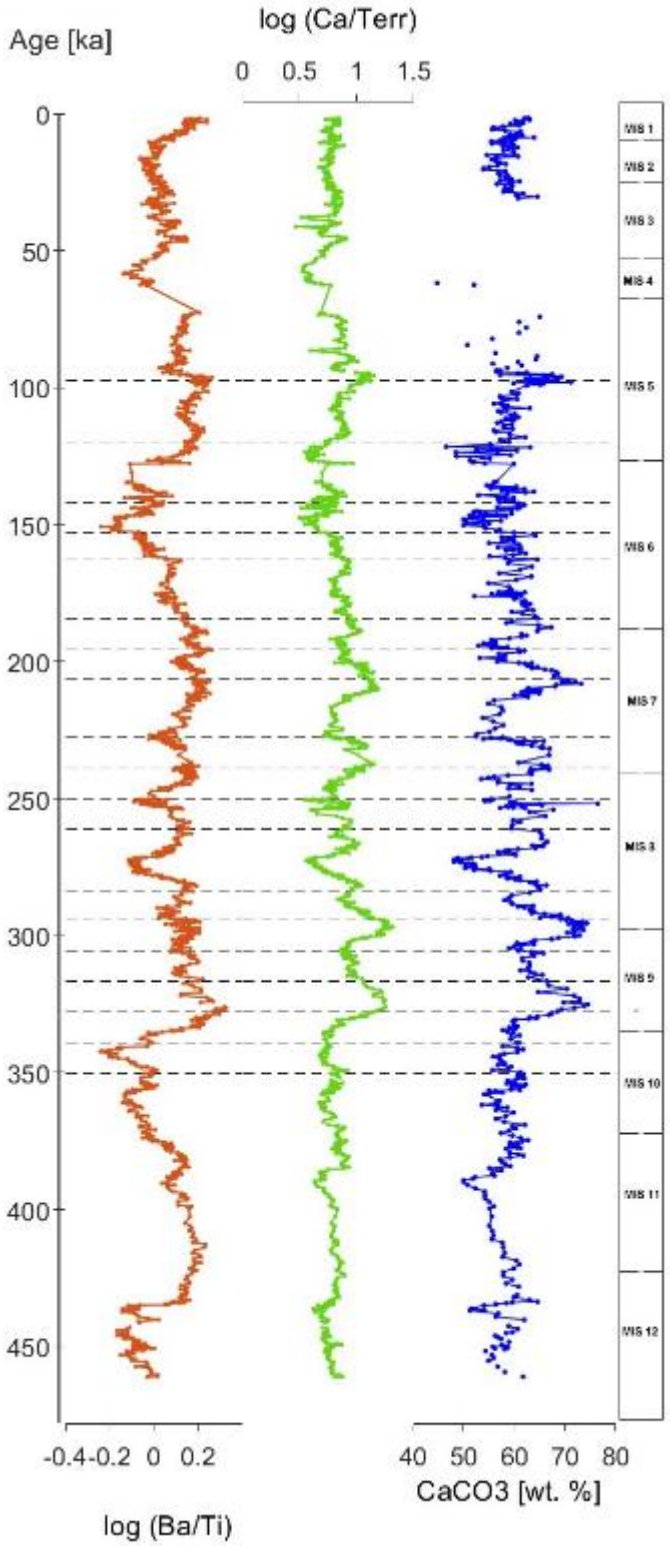

Figure 4.3| In the picture representation of the in-phase oscillation between log (Ca/Terr) (green), log (Ba/Ti) (orange), and $CaCO_3$ [wt. %] (blue), highlighted by the dot black lines. On the right side the MIS identified by Lisiecki & Raymo, (2005).

When the wind stress above the open ocean Site U1443 increases during the monsoon seasons, the surface-mixed layer increases in thickness, and consequently favourers an increase in primary productivity. Bolton et al., (2013), analyzed sediments from the Ninetyeast ridge of the Late Pleistocene and identified a half-precession (~11ka) signal in the record of $\Delta\,\delta^{18}O$ between surface and thermocline foraminifera, which is used as proxy of surface-mixed layer thickness. Therefore, the half-precession signal founded by Bolton et al., (2013), may explain the oscillations detected in the record of $CaCO_3$ wt.%, which happens to be every ~11ka.

4.2 The Interglacial Stage MIS 11

The $CaCO_3$ wt.% record from the Site U1443 during MIS 11 shows a steep decrease while primary productivity export rate and sedimentation rate maintained low constant values (Figure 4.2, 4.3). As no terrigenous dilution or decrease in primary productivity caused the decrease in the $CaCO_3$ [wt. %] is inferred that the dissolution might be responsible for the observed decrease. Data from Site 758 (Farrell & Janecek, 1991; Peterson & Prell, 1985) support this hypothesis as it is reported that the lysocline depth shoaled to ~2800m during the interglacial stage 11. The shallowing lysocline depth during the interglacial stage MIS 11 is therefore a possible response of the calcite homeostat mechanisms to the increased

ALK of the glacial deep ocean (Archer et al., 2000; Broecker, 1982; Brunelle et al., 2010; Yu et al., 2014). In fact according to these authors, in the case of a constant input of ALK in the ocean during low-sea level stands, the total ALK would increase due to the reduced $CaCO_3$ precipitation by the shallow-water system. Moreover, during glacial periods, atmospheric CO_2 would have been stored as DIC in the deep ocean. This is partially due to increased primary productivity in the Nord Atlantic Ocean and SubAntarctic Zone and the wider ice sheet coverage in the Southern Ocean, with the latter mechanically avoiding the $[CO_2]$ to escape from the ocean. The increase in DIC of the deep ocean would trigger dissolution of $CaCO_3$ in deep water sediments further increasing ALK. The carbonate homeostat system would balance the increase in ALK by decreasing the lysocline depth over 5 ka cycles. At the beginning of the deglacial, when the temperatures increase again and the ice sheet cover in the Southern Ocean decreases, the $[CO_2]$ gets newly released in the atmosphere. Hence, the deep ocean $[CO_3^{-2}]$ would increase and the carbonate compensation would balance the ALK input deepening the lysocline and increasing the preservation of $CaCO_3$. The build up of coral reef on shelves due to an increase in shallow water environments further decreased the ALK input and at the late deglacial, the $CaCO_3$ compensation

would again balance the ALK by shallowing the lysocline and causing increased dissolution of $CaCO_3$.

4.3 Revised size index response in Site U1443

At the beginning of interglacial MIS 9, the index shows that the system experienced increased preservation, while the glacial MIS 8 was characterized by increased dissolution (Figure 4.4). Meanwhile, the >150 μm (wt%) fraction record from Site 758, shows opposite results from the intervals analyzed (Figure 4.4) (Farrell & Janecek, 1991). Many are the possible reasons which could explain the different response in the two proxies. Firstly, they are based on different statements. While the >150 μm fraction (wt.%) measures the dissolution based on foraminiferal tests fragmentation, the revised size index considers the greater sensitivity of foraminifera (> 20 μm) dissolution related to the dissolution resistant coccolithophore (< 20 μm). In detail, the first is a measure of fragmentation of foraminifera, the second reflects the higher dissolution tendency for foraminifera calcite relative to coccolith calcite. Secondly, the >150 μm wt% in sediments does not depend only on the increased dissolution due to lower values $[CO_3^{-2}]$, but also on mechanical stress by deposit feeders and possible mechanical stress during washing in the laboratory (W. H. Berger, 1982). Moreover, the >150 μm wt% can

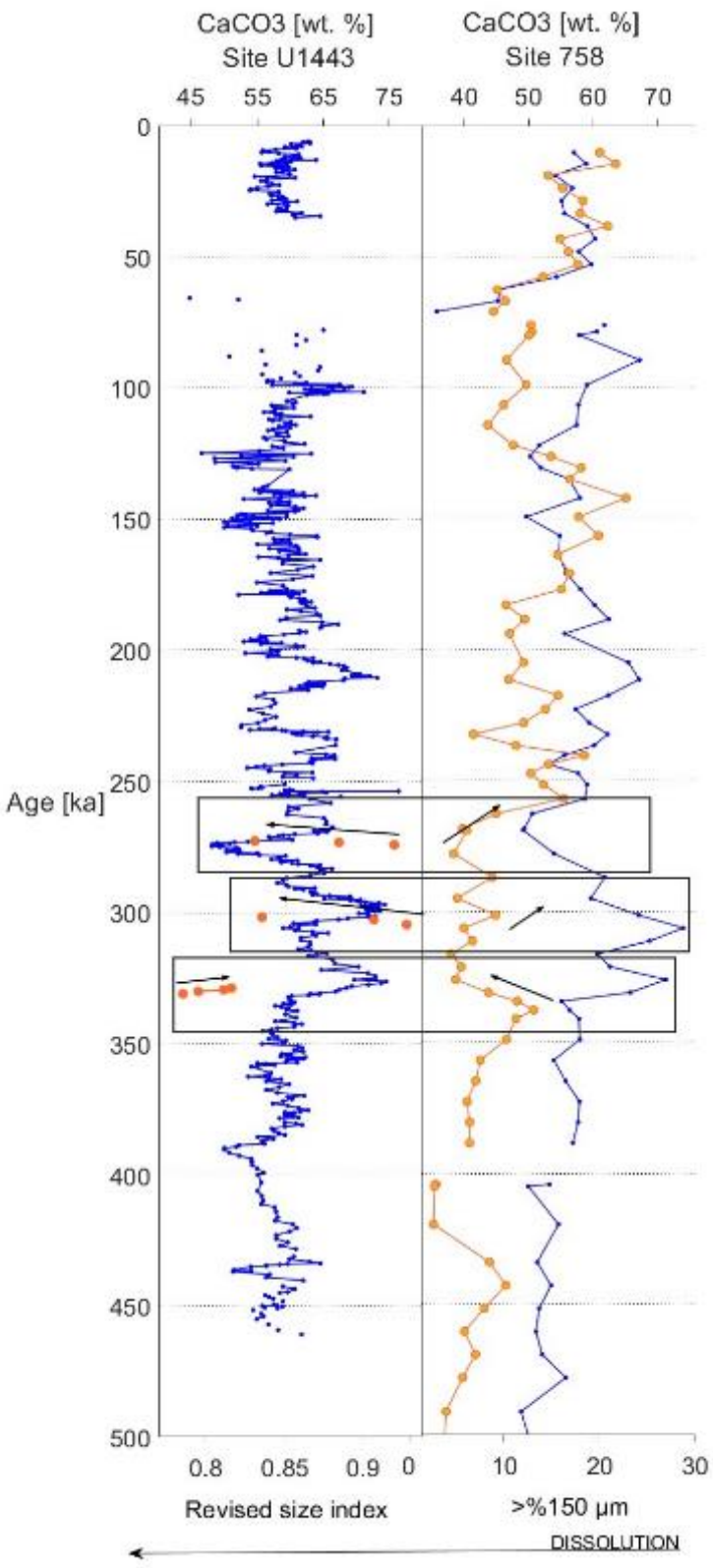

Figure 4.4| On the left panel the $CaCO_3$ [wt. %] (blue), and the revised size index from Site U1443 (orange). On the right panel the the $CaCO_3$ [wt. %] (blue), and >150µm [wt.%] fraction (orange) from Site 758. Both are plotted *vs* age. Data of Site 758 are taken from Farrell & Janecek, (1991).

be affected by the different, initial biogenic composition of $CaCO_3$ that was different between G-IG (Broecker & Clark, 2001). Meanwhile, the revised size index ratio, which considers the fraction of foraminifera on the total $CaCO_3$, doesn't suffer this possible bias. Beside these factors, there is also the possible weaker sensitivity of revised size index on sediments above lysocline, where the dissolution potentially is enough to cause the weakening of foraminifera test which then fragmented on the sea floor, but is potentially not enough to be detected by changes in the $CaCO_3$ % of the >20 μm fraction (Chiu & Broecker, 2008).

Chapther 5

CONCLUSIONS

The high-resolution reconstruction of the $CaCO_3$ sedimentation in the tropical Indian Ocean the Ninetyeast ridge (IODP Site U1443), spanning the last 460 ka, allows the conclusions summarised in the following:

(1) The total $CaCO_3$ [wt. %] does not exhibit any apparent relationship to the glacial/interglacial cycles as documented by fluctuations in planktic foraminiferal $\delta^{18}O$ from the same site, and by correlation with the benthic stack;

(2) During MIS 10 to MIS 1 dissolution does not play an evident role on the $CaCO_3$ sedimentation which was mainly controlled by primary productivity;

(3) The terrigenous dilution shows some effect on $CaCO_3$ [wt. %] during glacial periods;

(4) In the interval 350-198 ka the ~12 ka fluctuations in $CaCO_3$ [wt. %] reflect productivity changes of $CaCO_3$-secreting organisms in the water column;

(5) During the MIS 11 the $CaCO_3$ [wt. %] has experienced increased dissolution;

(6) The revised size index proxy is not in agreement with >150 μm wt% on sediments above lysocline, probably due to the lack of sensitivity in sediments collected above the lysocline.

References

Aitchison, J. (1982). The Statistical Analysis of Compositional Data. *Journal of the Royal Statistical Society: Series B (Methodological)*, *44*(2), 139–160. https://doi.org/https://doi.org/10.1111/j.2517-6161.1982.tb01195.x

Archer, D., Winguth, A., Lea, D., & Mahowald, N. (2000). What caused the glacial/interglacial atmospheric pCO2 cycles? *Reviews of Geophysics*, *38*(2), 159–189. https://doi.org/https://doi.org/10.1029/1999RG000066

Armstrong, H., & Brasier, M. (2013). *Microfossils*. John Wiley & Sons.

Arrhenius, G. (1952). Sediment cores from the east pacific. *Gff*, *75*(1), 115–118. https://doi.org/10.1080/11035895309454862

Arundhathy, M., Jyothibabu, R., Santhikrishnan, S., Albin, K. J., Parthasarathi, S., & Rashid, C. P. (2021). Coccolithophores: an environmentally significant and understudied phytoplankton group in the Indian Ocean. *Environmental Monitoring and Assessment*, *193*(3). https://doi.org/10.1007/s10661-020-08794-1

Bahk, J.-J., Um, I.-K., & Shin, K.-H. (2019). Contrasting developments of Pleistocene calcareous clay units in the middle Bengal Fan and their implications for paleoenvironmental changes. *Geosciences Journal*, *23*(6),

867–879. https://doi.org/10.1007/s12303-019-0012-0

Bassinot, F. C., Beaufort, L., Vincent, E., Labeyrie, L. D., Rostek, F., Müller, P. J., Quidelleur, X., & Lancelot, Y. (1994). Coarse fraction fluctuations in pelagic carbonate sediments from the tropical Indian Ocean: A 1500-kyr record of carbonate dissolution. *Paleoceanography*, *9*(4), 579–600. https://doi.org/https://doi.org/10.1029/94PA00860

Berger, A. (1988). Milankovitch Theory and climate. *Reviews of Geophysics*, *26*(4), 624–657. https://doi.org/https://doi.org/10.1029/RG026i004p00624

Berger, W. H. (1982). Increase of carbon dioxide in the atmosphere during deglaciation: the coral reef hypothesis. *Naturwissenschaften*, *69*(2), 87–88. https://doi.org/10.1007/BF00441228

Bolton, C. T., Chang, L., Clemens, S. C., Kodama, K., Ikehara, M., Medina-Elizalde, M., Paterson, G. A., Roberts, A. P., Rohling, E. J., Yamamoto, Y., & Zhao, X. (2013). A 500,000 year record of Indian summer monsoon dynamics recorded by eastern equatorial Indian Ocean upper water-column structure. *Quaternary Science Reviews*, *77*, 167–180. https://doi.org/https://doi.org/10.1016/j.quascirev.2013.07.031

Bolton, C. T., Gray, E., Kuhnt, W., Holbourn, A. E., Lübbers, J., Grant, K.,

Tachikawa, K., Marino, G., Rohling, E. J., & Sarr, A.-C. (2022). Secular and orbital-scale variability of equatorial Indian Ocean summer monsoon winds during the late Miocene. *Climate of the Past*, *18*(4), 713–738. https://doi.org/https://doi.org/10.5194/cp-18-713-2022

Bolton, C. T., & Stoll, H. M. (2013). Late Miocene threshold response of marine algae to carbon dioxide limitation. *Nature*, *500*(7464), 558–562. https://doi.org/10.1038/nature12448

Boudreau, B. P., Middelburg, J. J., & Luo, Y. (2018). The role of calcification in carbonate compensation. *Nature Geoscience*, *11*(12), 894–900. https://doi.org/https://doi.org/10.1038/s41561-018-0259-5

Broecker, W. S. (1982). Ocean chemistry during glacial time. *Geochimica et Cosmochimica Acta*, *46*(10), 1689–1705. https://doi.org/https://doi.org/10.1016/0016-7037(82)90110-7

Broecker, W. S. (2003). The Oceanic CaCO 3 Cycle. In *Treatise on geochemistry 6*.

Broecker, W. S. (2008). A need to improve reconstructions of the fluctuations in the calcite compensation depth over the course of the Cenozoic. *Paleoceanography*,*23*(1).

https://doi.org/https://doi.org/10.1029/2007PA001456

Broecker, W. S., & Clark, E. (2001). Reevaluation of the CaCO3 size index paleocarbonate ion proxy. *Paleoceanography*, *16*(6), 669–671. https://doi.org/https://doi.org/10.1029/2001PA000660

Brunelle, B. G., Sigman, D. M., Jaccard, S. L., Keigwin, L. D., Plessen, B., Schettler, G., Cook, M. S., & Haug, G. H. (2010). Glacial/interglacial changes in nutrient supply and stratification in the western subarctic North Pacific since the penultimate glacial maximum. *Quaternary Science Reviews*, *29*(19–20), 2579–2590.

https://doi.org/https://doi.org/10.1016/j.quascirev.2010.03.010

Chiu, T.-C., & Broecker, W. S. (2008). Toward better paleocarbonate ion reconstructions: New insights regarding the CaCO3 size index. *Paleoceanography*, *23*(2).

https://doi.org/https://doi.org/10.1029/2008PA001599

Clemens, S. C., Kuhnt, W., LeVay, L. J., Anand, P., Ando, T., Bartol, M., Bolton, C. T., Ding, X., Gariboldi, K., & Giosan, L. (2016a). Expedition 353 summary. *Clemens, SC, Kuhnt, W., LeVay, LJ, and the Expedition*, *353*.

Clemens, S. C., Kuhnt, W., LeVay, L. J., Anand, P., Ando, T., Bartol, M., Bolton,

C. T., Ding, X., Gariboldi, K., & Giosan, L. (2016b). Site U1443. *Clemens, SC, Kuhnt, W., LeVay, LJ, the Expedition*, *353*, 1–41.

Colleoni, F., Masina, S., Negri, A., & Marzocchi, A. (2012). Plio–Pleistocene high–low latitude climate interplay: A Mediterranean point of view. *Earth and Planetary Science Letters*, *319–320*, 35–44.

https://doi.org/https://doi.org/10.1016/j.epsl.2011.12.020

Cullen, J. L., & Prell, W. L. (1984). Planktonic foraminifera of the northern Indian Ocean: Distribution and preservation in surface sediments. *Marine Micropaleontology*, *9*(1), 1–52. https://doi.org/https://doi.org/10.1016/0377-8398(84)90022-7

Curray, J. R., Emmel, F. J., Moore, D. G., & Raitt, R. W. (1982). *Structure, Tectonics, and Geological History of the Northeastern Indian Ocean BT - The Ocean Basins and Margins: The Indian Ocean* (A. E. M. Nairn & F. G. Stehli (eds.); pp. 399–450). Springer US. https://doi.org/10.1007/978-1-4615-8038-6_9

Dickson, A. G. (1981). An exact definition of total alkalinity and a procedure for the estimation of alkalinity and total inorganic carbon from titration data. *Deep Sea Research Part A. Oceanographic Research Papers*, *28*(6), 609–623.

https://doi.org/https://doi.org/10.1016/0198-0149(81)90121-7

Divakar Naidu, P., & Malmgren, B. A. (1999). Quaternary carbonate record from the equatorial Indian Ocean and its relationship with productivity changes. *Marine Geology*, *161*(1), 49–62. https://doi.org/https://doi.org/10.1016/S0025-3227(99)00055-9

Divakar Naidu, P., Malmgren, B. A., & Bornmalm, L. (1993). Quaternary history of calcium carbonate fluctuations in the western equatorial Indian Ocean (Somali Basin). *Palaeogeography, Palaeoclimatology, Palaeoecology*, *103*(1), 21–30. https://doi.org/https://doi.org/10.1016/0031-0182(93)90048-N

Farrell, J. W., & Janecek, T. R. (1991). (Appendix A) Comparison of CaCO3 data generated at Brown University and ODP Shipboard Laboratories, ODP Site 121-758. In *In supplement to: Farrell, JW; Janecek, TR (1991): Late Neogene paleoceanography and paleoclimatology of the northeast Indian Ocean (Site 758). In: Weissel, J; Peirce, J; Taylor, E; et al. (eds.), Proceedings of the Ocean Drilling Program, Scientific Resu*. PANGAEA. https://doi.org/10.1594/PANGAEA.759089

Fiadeiro, M. (1980). The alkalinity of the deep Pacific. *Earth and Planetary*

Science Letters, *49*(2), 499–505. https://doi.org/https://doi.org/10.1016/0012-821X(80)90090-4

Gebregiorgis, D., Giosan, L., Hathorne, E. C., Anand, P., Nilsson-Kerr, K., Plass, A., Lückge, A., Clemens, S. C., & Frank, M. (2020). What Can We Learn From X-Ray Fluorescence Core Scanning Data? A Paleomonsoon Case Study. *Geochemistry, Geophysics, Geosystems*, *21*(2), e2019GC008414. https://doi.org/https://doi.org/10.1029/2019GC008414

International Atomic Energy Agency. (2003). Collection and preparation of bottom sediment samples for analysis of radionuclides and trace elements. *Atomic Energy*, *July*, 1–130.

Kawagata, S., Hayward, B. W., & Gupta, A. K. (2006). Benthic foraminiferal extinctions linked to late Pliocene-Pleistocene deep-sea circulation changes in the northern Indian Ocean (ODP Sites 722 and 758). *Marine Micropaleontology*, *58*(3), 219–242.

https://doi.org/10.1016/j.marmicro.2005.11.003

Lisiecki, L. E., & Raymo, M. E. (2005). A Pliocene-Pleistocene stack of 57 globally distributed benthic δ18O records. *Paleoceanography*, *20*(1). https://doi.org/https://doi.org/10.1029/2004PA001071

Lübbers, J., Kuhnt, W., Holbourn, A. E., Bolton, C. T., Gray, E., Usui, Y., Kochhann, K. G. D., Beil, S., & Andersen, N. (2019). The Middle to Late Miocene "Carbonate Crash" in the Equatorial Indian Ocean. *Paleoceanography and Paleoclimatology*, *34*(5), 813–832. https://doi.org/https://doi.org/10.1029/2018PA003482

Martin, J. H., Fitzwater, S. E., Gordon, R. M., Hunter, C. N., & Tanner, S. J. (1993). Iron, primary production and carbon-nitrogen flux studies during the JGOFS North Atlantic Bloom Experiment. *Deep Sea Research Part II: Topical Studies in Oceanography*, *40*(1–2), 115–134. https://doi.org/https://doi.org/10.1016/0967-0645(93)90009-C

Maslin Mark, A., & Ridgwell Andy, J. (2005). Mid-Pleistocene revolution and the 'eccentricity myth.' *Geological Society, London, Special Publications*, *247*(1), 19–34. https://doi.org/10.1144/GSL.SP.2005.247.01.02

Milliman, J. D., Troy, P. J., Balch, W. M., Adams, A. K., Li, Y.-H., & Mackenzie, F. T. (1999). Biologically mediated dissolution of calcium carbonate above the chemical lysocline? *Deep Sea Research Part I: Oceanographic Research Papers*, *46*(10), 1653–1669. https://doi.org/https://doi.org/10.1016/S0967-0637(99)00034-5

Naidu, P. D. (1991). Glacial to interglacial contrasts in the calcium carbonate content and influence of Indus discharge in two eastern Arabian Sea cores. *Palaeogeography, Palaeoclimatology, Palaeoecology*, *86*(3), 255–263. https://doi.org/https://doi.org/10.1016/0031-0182(91)90084-5

Naik, S. S., & Naidu, P. D. (2016). Carbonate preservation during the `mystery interval' in the northern Indian Ocean. *Geochemical Journal*, *50*(4), 357–362. https://doi.org/10.2343/geochemj.2.0420

Öğretmen, N., Cipollari, P., Frezza, V., Faranda, C., Karanika, K., Gliozzi, E., Radeff, G., & Cosentino, D. (2018). Evidence for 1.5 km of Uplift of the Central Anatolian Plateau's Southern Margin in the Last 450 kyr and Implications for Its Multiphased Uplift History. *Tectonics*, *37*(1), 359–390. https://doi.org/https://doi.org/10.1002/2017TC004805

Pearson, K. (1896). VII. Mathematical contributions to the theory of evolution.—III. Regression, heredity, and panmixia. *Philosophical Transactions of the Royal Society of London. Series A, Containing Papers of a Mathematical or Physical Character*, *187*, 253–318. https://doi.org/https://doi.org/10.1098/rsta.1896.0007

Peterson, L. C., & Prell, W. L. (1984). Carbonate dissolution in Recent sediments

of the eastern equatorial Indian Ocean: Preservation patterns and carbonate loss above the lysocline. *Marine Geology*, *64*(3–4), 259–290. https://doi.org/10.1016/0025-3227(85)90108-2

Peterson, L. C., & Prell, W. L. (1985). Carbonate preservation and rates of climatic change: an 800kyr record from the Indian Ocean. *The Carbon Cycle and Atmospheric CO*, *32*, 251–269. https://doi.org/10.1029/gm032p0251

Petit, J.-R., Jouzel, J., Raynaud, D., Barkov, N. I., Barnola, J.-M., Basile, I., Bender, M., Chappellaz, J., Davis, M., & Delaygue, G. (1999). Climate and atmospheric history of the past 420,000 years from the Vostok ice core, Antarctica. *Nature*, *399*(6735), 429–436.

https://doi.org/https://doi.org/10.1038/20859

Reijmer, J. J. G. (2021). Marine carbonate factories: Review and update. *Sedimentology*, *68*(5), 1729–1796.

https://doi.org/https://doi.org/10.1111/sed.12878

Rothwell, R. G. (2004). Deep ocean pelagic oozes. *Encyclopedia of Geology*.

Sarmiento, J. L., & Gruber, N. (2006). *Ocean Biogeochemical Dynamics*. Princeton University Press.

https://doi.org/https://doi.org/10.1515/9781400849079

Sigman, D. M., & Boyle, E. A. (2000). Glacial/interglacial variations in atmospheric carbon dioxide. *Nature*, *407*(6806), 859–869. https://doi.org/10.1038/35038000

Smith, S. V, & Mackenzie, F. T. (2016). The Role of CaCO3 Reactions in the Contemporary Oceanic CO2 Cycle. *Aquatic Geochemistry*, *22*(2), 153–175. https://doi.org/10.1007/s10498-015-9282-y

Spearman, C. (1961). *The proof and measurement of association between two things.*

Tadamichi, O. (1969). Biostratigraphy and Isotopic Paleotemperature of some Deep-Sea Cores from the Indian Ocean. *The Science Reports of the Tohoku University. Second Series, Geology = 東北大学理科報告. 地質学*, *41*(2), 129-A8. https://cir.nii.ac.jp/crid/1571417126930954880.bib?lang=ja

Tyrrell, T., & Young, J. R. (2009). *Coccolithophores, Encyclopedia of Ocean Sciences*. Academic Press.

Weiss, R. F. (1974). Carbon dioxide in water and seawater: the solubility of a non-ideal gas. *Marine Chemistry*, *2*(3), 203–215.

https://doi.org/https://doi.org/10.1016/0304-4203(74)90015-2

Weissel, J. et al. (1991). *24 . ORGANIC AND CARBONATE CARBON ACCUMULATION ON BROKEN RIDGE AND NINETYEAST RIDGE, CENTRAL INDIAN OCEAN1*. *121*.

Weltje, G. J., & Tjallingii, R. (2008). Calibration of XRF core scanners for quantitative geochemical logging of sediment cores: Theory and application. *Earth and Planetary Science Letters*, *274*(3), 423–438. https://doi.org/https://doi.org/10.1016/j.epsl.2008.07.054

Wood, M., Hayes, C. T., & Paytan, A. (2023). Global Quaternary Carbonate Burial: Proxy- and Model-Based Reconstructions and Persisting Uncertainties. *Annual Review of Marine Science*, *15*(1), 277–302. https://doi.org/10.1146/annurev-marine-031122-031137

Yadav, R., Naik, S. S., & Naidu, P. D. (2022). Contrasts in calcium carbonate dissolution above the lysocline in the equatorial Indian Ocean over the last ~40 ka. *Marine Geology*, *444*, 106717.

https://doi.org/https://doi.org/10.1016/j.margeo.2021.106717

Yu, J., Anderson, R. F., Jin, Z., Rae, J. W. B., Opdyke, B. N., & Eggins, S. M. (2013). Responses of the deep ocean carbonate system to carbon

reorganization during the Last Glacial–interglacial cycle. *Quaternary Science Reviews*, *76*, 39–52.

https://doi.org/https://doi.org/10.1016/j.quascirev.2013.06.020

Yu, J., ANDERSON, R. F., & ROHLING, E. J. (2014). Deep Ocean Carbonate Chemistry and Glacial-Interglacial Atmospheric CO_2 Changes. *Oceanography*, *27*(1), 16–25. http://www.jstor.org/stable/24862115

Zeebe, R. E. (2012). History of seawater carbonate chemistry, atmospheric CO 2, and ocean acidification. *Annual Review of Earth and Planetary Sciences*, *40*(141), 2012. https://doi.org/https://doi.org/10.1146/annurev-earth-042711-105521

Zeebe, R. E., & Wolf-Gladrow, D. (2001). *CO2 in seawater: equilibrium, kinetics, isotopes* (Issue 65). Gulf Professional Publishing.

Zhang, H., Luo, Y., Yu, J., Zhang, L., Xiang, R., Yu, Z., & Huang, H. (2022). Indian Ocean sedimentary calcium carbonate distribution and its implications for the glacial deep ocean circulation. *Quaternary Science Reviews*, *284*, 107490. https://doi.org/https://doi.org/10.1016/j.quascirev.2022.107490